Characterizing Near-Nadir and Low Incidence Ka-Band SAR Backscatter From Wet Surfaces and Diverse Land Covers

Jessica V. Fayne, *Member, IEEE*, Laurence C. Smith, Tien-Hao Liao, Lincoln H Pitcher, Michael Denbina, Albert C. Chen, Marc Simard, Curtis W. Chen, and Brent A. Williams, *Member, IEEE*

***Abstract*—The Surface Water and Ocean Topography (SWOT) satellite and AirSWOT airborne instrument are the first imaging radar-altimeters designed with near-nadir and low incidence, 35.75 GHz Ka-band InSAR for mapping terrestrial water storage variability. Remotely sensed surface water extents are crucial for assessing such variability but are confounded by emergent and inundated vegetation along shorelines. However, because SWOT-like measurements are novel, there remains some uncertainty in the ability to detect certain land and water classes. This study examines the likelihood of misclassification between 15 land cover types and develops the Ka-band Phenomenology Scattering (KaPS) model to simulate changes to Ka-band backscatter as a result of changing surface water fraction and surface structure, including vegetation morphology and water surface waves. Using a separability metric, the study finds that water is five times more distinct compared with dry land classes, but has the potential to be confused with littoral zone and wet soil cover types. The KaPS scattering model simulates AirSWOT backscatter for incidence angles 1–27°, identifying the conditions under which open water is likely to be confused with littoral zone and wet soil cover types. KaPS characterization of the sensitivity of near-nadir and low incidence Ka-band SAR to small changes in both wet area fraction and surface structure enables a more nuanced classification of inundation area. These results provide additional confidence in the ability of SWOT to classify water inundation extent and open the door for novel hydrological and ecological applications of future Ka-band SAR missions.**

Manuscript received 10 April 2023; revised 2 July 2023 and 8 August 2023; accepted 2 September 2023. Date of publication 20 September 2023; date of current version 6 December 2023. This work was supported in part by NASA Future Investigators in Earth and Space Science and Technology (FINESST) graduate fellowship under Grant 80NSSC19K1377, in part by NASA Surface Water and Ocean Topography Science Team Program under Grant 80NSSC20K1144 managed by Nadya Vinogradova-Shiffer, and in part by the NASA Terrestrial Ecology under Grant 80NSSC22K1237 managed by Hank Margolis. *(Corresponding author: Jessica V. Fayne.)*

Jessica V. Fayne is with the Earth and Environmental Sciences, University of Michigan, Ann Arbor, MI 48109 USA (e-mail: jfayne@umich.edu).

Laurence C. Smith is with the Department of Earth, Environmental, and Planetary Sciences, Brown University, Providence, RI 02912 USA (e-mail: laurence_smith@brown.edu).

Tien-Hao Liao is with the Department of Electrical Engineering, National Taipei University of Technology, Taipei 10608, Taiwan (e-mail: thliao@ntut.edu.tw).

Lincoln H Pitcher is with the Cooperative Institute for Research and Environmental Sciences (CIRES), University of Colorado at Boulder, Boulder, CO 80309 USA (e-mail: lincoln.pitcher@colorado.edu).

Michael Denbina, Albert C. Chen, Marc Simard, Curtis W. Chen, and Brent A. Williams are with the Radar Science and Engineering, NASA Jet Propulsion Laboratory, Pasadena, CA 91011 USA (e-mail: michael.w.denbina@jpl.nasa.gov; albert.c.chen@jpl.nasa.gov; marc.simard@jpl.nasa.gov; curtis.w.chen@jpl.nasa.gov; brent.a.williams@jpl.nasa.gov).

Digital Object Identifier 10.1109/JSTARS.2023.3317502

***Index Terms*—Hydrology, Ka-band, land cover, surface moisture, surface structure, surface water, Surface Water and Ocean Topography (SWOT), synthetic aperture radar, vegetation.**

I. Introduction

THE inundation extent and water surface elevation of inland lakes, rivers, and wetlands are critical remote sensing measurements for monitoring the terrestrial hydrological cycle [1], [2], [3], [4], [5], [6], [7], [8]. Remote sensing of inundation extent is complicated by riparian vegetation along shorelines and aquatic vegetation in shallow or flooded areas, especially with optical sensors [9], [10], [11]. Both optical and microwave methods underestimate inundation extent where vegetation density outweighs observable water fraction [10] or when classification methods prioritize open water classification accuracy over total extent [11]. The study of aquatic vegetation remains an active area of research for both active and passive remote sensing examinations.

While long-wavelength, high-incidence angle radars (especially L band) are traditionally favored for hydrological applications due to their superior vegetation penetration–and in some cases, ground penetration [13], [14], [15], [16]–low-incidence angle short-wavelength radar systems can also measure water extent and water surface elevation effectively [17], [18]. Because Ka-band SAR can be highly sensitive to both liquid surface water and vegetation, it is useful for terrestrial hydrology and ecological studies. Ka-band radars are sensitive to fine-scale scattering features (i.e., on the order of their wavelength, ∼8.4 mm), for example, having better capabilities of detecting small standing and capillary waves on open water surfaces or the presence of non-woody emergent and/or floating aquatic plants. The short Ka-band wavelengths therefore have the potential to reveal different physical properties of wet and/or vegetated surfaces than conventional longer-wavelength C-, L-, and P-band radars. Nonetheless, to what extent such technologies can discriminate between diverse surface covers and differing moisture contents remains an area of investigation [19], [20], [21].

The Surface Water Ocean Topography (SWOT) satellite mission,[1] developed by NASA and CNES with contributions from CSA and UKSA, launched on December 16, 2022, uses

[1] [Online]. Available: https://swot.jpl.nasa.gov/

Ka-band interferometry to produce the first swath altimetric measurements of surface water from space [12], [22], [23]. For land surface hydrology, the goal of the SWOT mission is to enable global, submonthly (11 to 21-day) mapping of freshwater storage and river discharge for lakes as small as $(250\ \text{m})^2$ and rivers as narrow as 100 m [24]. To achieve this, open water surfaces must be consistently identifiable in SWOT Ka-band imagery. Based on theoretical modeling and observations, accurate open water identification is anticipated due to strong backscatter returns from open water surfaces at near-nadir incidence angles (0.6°–4.1°) [18], [19], [25], [26], [27]. However, preliminary observations of near-nadir and low incidence (0°–30°) Ka-band backscatter from AirSWOT, an airborne swath altimeter, suggest significant real-world complexity, including relatively low backscatter returns from portions of some open water surfaces, and higher returns from some classes of land surfaces [28]. Early AirSWOT assessments also report strong radar returns, similar to expected open water returns, from wetland vegetation and moist bare soils [28], [29], [30]. Such reports have raised concern within the SWOT science community about possible misclassifications of surface water [29], [31], and have prompted a desire for improved understanding and modeling of Ka-band backscatter returns over inland water bodies and diverse land covers. A March 24, 2023 press release from CNES demonstrated one of the first SWOT backscatter images over Toulouse, France, highlighting bright scattering over land features and good differentiation of water bodies.[2]

Software for analyzing radar backscatter (e.g., PolSARProSim, SNAP) are often developed for longer wavelengths (>5 cm), but to the authors' knowledge, no publicly available software can readily be used to simulate Ka-band scattering for hydrology applications, including surface water and various land covers. Several approaches have been developed to model microwave scattering, including theoretical approaches such as the Kirchhoff Approximation (KA), Geometric Optics (GO), and Physical Optics (PO) models [32], [33], [34], [35] are rigorous but computationally intensive for complex terrain. This is especially true when the terrain has diverse surface cover, including bare soil, vegetation, and water, with a wide range of incidence angles. Empirical and semi-empirical models often require dual- or quad-polarized observations (HH, VV, VH, and HV) and assume small surface roughness and structural variations relative to the wavelength [36], [37].

Some of these theoretical and empirical methods have been applied to Ka-band low-incidence applications [21] for a few terrestrial targets [38] as well as liquid water [39], [40]. However, many of these approaches have shortcomings when applying to SWOT-like incidence angles, resolutions, and/or terrestrial target classes (inland water as well as spatially nonhomogeneous land types). Simulators for SWOT data, developed by NASA-JPL and demonstrated in [41], use known static parameters such as topography, land cover, and scaled, spatially homogenous wind speed to predict scattering variability based on 5 km resolution Ka-band radar data from the Global Precipitation Measurement (GPM) satellite.

In support of the SWOT simulator and to provide an additional foundation for future Ka-band phenomenology research, this article develops a simple empirical scattering model based on the statistical relationships between remotely sensed datasets. The study assumes that such a model should include surface dielectric properties, which are captured using volumetric soil moisture, and surface geometry, captured using foliage height diversity (FHD) or waveform "complexity," a metric describing the vertical heterogeneity of a LiDAR surface target (including vegetated and non-vegetated surfaces). Because the 8.4 mm wavelength is much smaller than many of the observed surface features, all features are considered to be "rough" in the electromagnetic sense, and therefore the study examines larger "structural" geometric features, referring to intermediate-scale textural features such as leaves and branches (represented by the FHD complexity product). We do not apply any model to convert moisture to dielectric values physically, nor do we produce a physical model of electromagnetic scale roughness. The dielectric component of radar backscatter modeling often focuses on moisture and ignores temperature (with some exceptions related to the dielectric change due to the phase change of snow, ice, or permafrost [42], [43], [44], [45], [46]). Because the AirSWOT data does not have observations of frozen conditions, temperature, and phase change influences are not assessed in this study.

Traditional SAR and InSAR systems for land surface observations are typically C, S, L, or P-band (0.05–1 m wavelengths), which are less sensitive to fine-scale surface features such as tree leaves and short, non-woody plants. In contrast, shorter wavelengths from X, Ku, and Ka-band are more sensitive to vegetative features. Since the primary objective of these systems is to investigate land properties [47], [48], [49], [50], they typically use higher incidence angles, averaging around 30° (±5°) and up to 50° [51], that exhibit higher backscatter over land than over open water surfaces. In contrast, AirSWOT and SWOT use lower incidence angles, producing higher backscatter returns over water than the surrounding land [18], [19], [52], [53]. AirSWOT acquires data in two swaths: an inner swath having a near-nadir incidence angle range similar to SWOT (0.6–4.1°), and an outer swath covering part of the inner range and extends to low incidence angles (≲3°–27°) [18], [25]. Both swaths use vertical polarization for transmit and receive (single pol: VV). As the inner swath data has not been made publicly available for research, the data in this study and those reported in previous studies [54], [55], [56], [57], [58] are from the outer swath, and thus the range of incidence angles is large enough that the water backscattering varies significantly from one edge of the swath to the other, within the observed range of incidence angles. In this article, "near-nadir" refers to the incidence angle range 0°–10°, while "low incidence" refers to the incidence angle range 10°–30°, though each AirSWOT image includes both ranges (≲3°–27°).

In addition, it is critical to identify regions with mixed pixels containing backscatter contributions from both land and water,

[2][Online]. Available: [https://presse.cnes.fr/en/swot-water-tracking-satellite-sends-back-first-stunning-views, accessed March 24, 2023].

as these may lead to classification errors and phase shifts resulting in elevation retrieval errors [52], [58]. Surface water extent and resultant phase errors have implications for developing and validating future Ka-band instruments and future applications and validation of AirSWOT and SWOT. To assess these phenomenological sources of error, the study identifies backscatter sensitivities to varying surface types and evaluates under what conditions water surfaces may be confused with other land types, which additionally has implications for mixed pixels at more coarse spatial scales than observed with AirSWOT.

This study advances physical understanding and modeling of Ka-band backscattering response across a diverse range of surface moisture conditions and land cover types by analyzing an extensive archive of AirSWOT Ka-band SAR data acquired across Alaska and western Canada for the NASA Arctic-Boreal Vulnerability Experiment (ABoVE) [59]. First, the study determines the separability of near-nadir and low-incidence Ka-band SAR backscatter for wet surfaces and diverse land covers to assess retrievals of water surface area. Next, an empirical investigation is conducted, examining the influence of volumetric surface moisture and foliage height diversity (FHD: form/geometry/complexity) on Ka-band surface scattering. These relationships are then used to develop a model to simulate near-nadir and low-incidence Ka-band surface scattering, called Ka-band Phenomenology Scattering (KaPS) model, developed to also simulate spatial and temporal variations in Ka-band backscatter caused by changing surface moisture and structure. The study concludes with a broader discussion of the study's implications for hydrological Ka-band remote sensing and backscatter modeling.

II. Data and Methods

A. Data

The AirSWOT Ka-band SWOT Phenomenology Airborne Radar (KaSPAR) is a multiantenna, Ka-band wide-swath altimeter that uses InSAR processing to produce 3.6 m horizontal resolution maps of water and land surface elevations. AirSWOT was developed as an airborne complement to SWOT to test and design radar and InSAR algorithms and to understand surface phenomenological interactions at Ka band [18], [25]. This study uses AirSWOT's outer swath data products, spanning near-nadir to low incidence angles (∼3°–27°). The radar data products used in the analysis include: 1) incidence angle; 2) noise subtracted and 3) calibrated backscatter, 4) signal-to-noise ratio (SNR), and 5) irregular grid geolocation (lat-lon-height-error LLHE) datasets processed at the NASA Jet Propulsion Laboratory (JPL) [59]. The published data are multilooked and geocoded to produce final map products having a nominal pixel spacing of 3.6 m, with flight acquisition dates between July 8 and August 17, 2017. Coverage of the AirSWOT ABoVE flights are shown in Fig. 1. For technical descriptions of these data products and the AirSWOT instrument configuration see [25], [59]. The collection spans a 23° latitude gradient and captures a 17 cm seasonal hydrologic drawdown [52]. These observations and findings enable the study of temporal variability in the Ka-band backscatter due to surface moisture dynamics. With the exception of the SNR and LLHE radar products, these products are freely available for download (https://daac.ornl.gov/cgi-bin/dsviewer.pl?ds_id = 1646 [52], [59]).

For brevity, the term "backscatter" here refers to the "near-nadir and low incidence Ka-band backscatter" from the AirSWOT platform; and the term "Ka-band" is used to refer to the 35.75 GHz frequency (∼8.4 mm wavelength) of AirSWOT and SWOT. For detailed specifications of the AirSWOT and SWOT instruments see [18], [19], [25], [26], [54], [55], [56], [58].

The 2014 Arctic Boreal Vulnerability Experiment ABoVE Annual Dominant Land Cover (ADLC) [60] product is used as a land cover reference. The 30 m ADLC is derived from Landsat-7 Thematic Mapper imagery and contains the annual dominant plant functional type represented as fifteen land cover classes (evergreen forest, deciduous forest, mixed forest, woodland, low shrub, tall shrub, open shrub, herbaceous, tussock tundra, sparsely vegetated, fen, bog, shallows/littoral, barren and water). Previous high-frequency scattering analyses have been limited to water surfaces and broad vegetation types [53], [61], [62], [63]; using the ADLC enables a more detailed examination of the influences of surface variations and land cover variability on Ka-band backscatter. The extensive coverage area and moderate resolution afforded by the Landsat-based classification make it a very useful reference dataset to analyze Ka-band scattering coefficients for a more diverse range of land cover types than has been previously published.

The NOAA Soil Moisture Products System (SMOPS) blended radiometer volumetric soil moisture percentage product [64] is used to assess broad-scale variations in surface moisture across the 23° of latitude and 17 cm hydrologic drawdown with a 25 km spatial resolution and a daily temporal resolution.

Airborne full-waveform LiDAR data collected from the Land Vegetation and Ice Sensor (LVIS) [65] are used to assess the influence of surface geometry (FHD) on Ka-band scattering. The LiDAR data are collected within days of the AirSWOT flights and provide full-waveform analysis of surface characteristics. These full-waveform pulses are capable of penetrating canopies, providing detailed information on canopy and forest structure in diverse environments with reflected power at continuous elevation points along the height of the feature [66]. Unlike conventional LiDAR systems which might maintain up to 10 discrete points within a footprint, LVIS' full-waveform system may keep as many as 1000 points, describing a continuous distribution of infrared scattered energy along the vertical profile for each point. Complexity is the specific LVIS product used for this analysis [representing FHD and similar to the leaf area index (LAI)], which is included in the LVIS L2 Geolocated Surface Elevation Product dataset ([67] https://nsidc.org/data/ABLVIS2), providing a single-value metric to describe vertical heterogeneity and density of features along the profile [68]. Complexity is proportional to the integration of the normalized returned LiDAR signal over segments of the vertical profiles. (For the full explanation and equations, see the algorithm theoretical basis document describing vertical profile metrics [68], particularly Fig. 3 and equations 11–12). Low complexity values usually

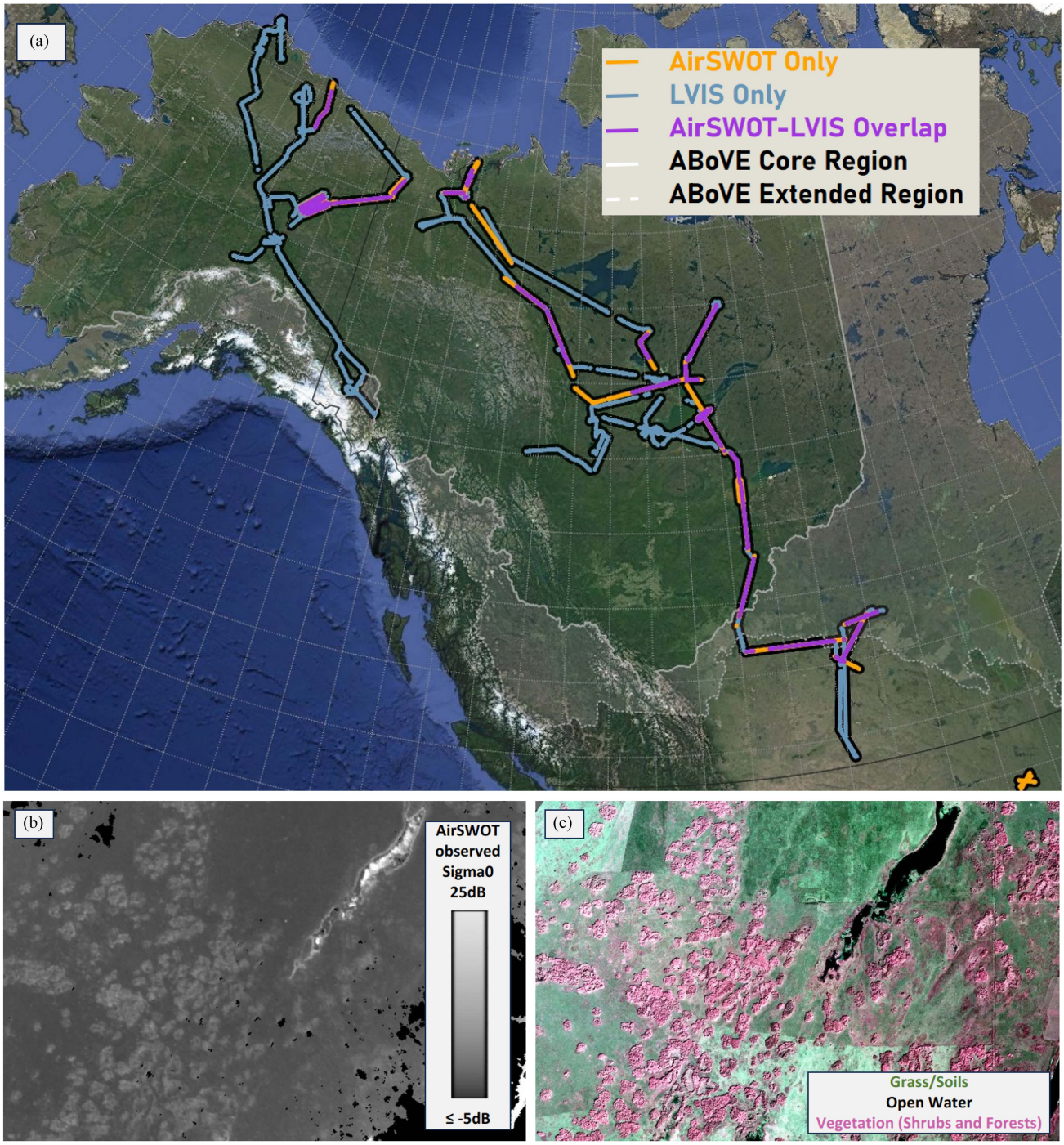

Fig. 1. (a) Study area of the 2017 ABoVE airborne data collection of AIrSWOT and LVIS data. AirSWOT data was collected between July 8, and August 17, 2017; Land Vegetation and Ice Sensor (LVIS) data was collected within days of the AirSWOT northbound Flights, from June 29 to July 18, 2017. Vegetation structural scattering contributions to AirSWOT Ka-band backscatter data are assessed using full-waveform data collected from LVIS. (b) An example of a Ka-band backscatter image containing tree stands among agricultural fields and lakes, near the North Saskatchewan River, in Saskatchewan, Canada. The tree stands are brighter than the surrounding vegetation. Water is much brighter than other surfaces. C) A reference color-infrared image acquired from the CIR camera onboard the AirSWOT platform. With the false-color mapping, the tree stands are visible in red, pink, and white tones.

indicate flat ground or water surfaces, while high complexity values usually indicate dense canopies. The nominal pulse footprint spacing is 10 m, but the data has been gridded and resampled in this examination to 20 m, to provide smoother coverage and transitions over irregularly missing data.

B. Methods

1) Separability of Near-Nadir and Low Incidence ka-Band SAR Backscatter for Wet Surfaces and Diverse Land Covers: To calculate the extent to which open water, emergent aquatic

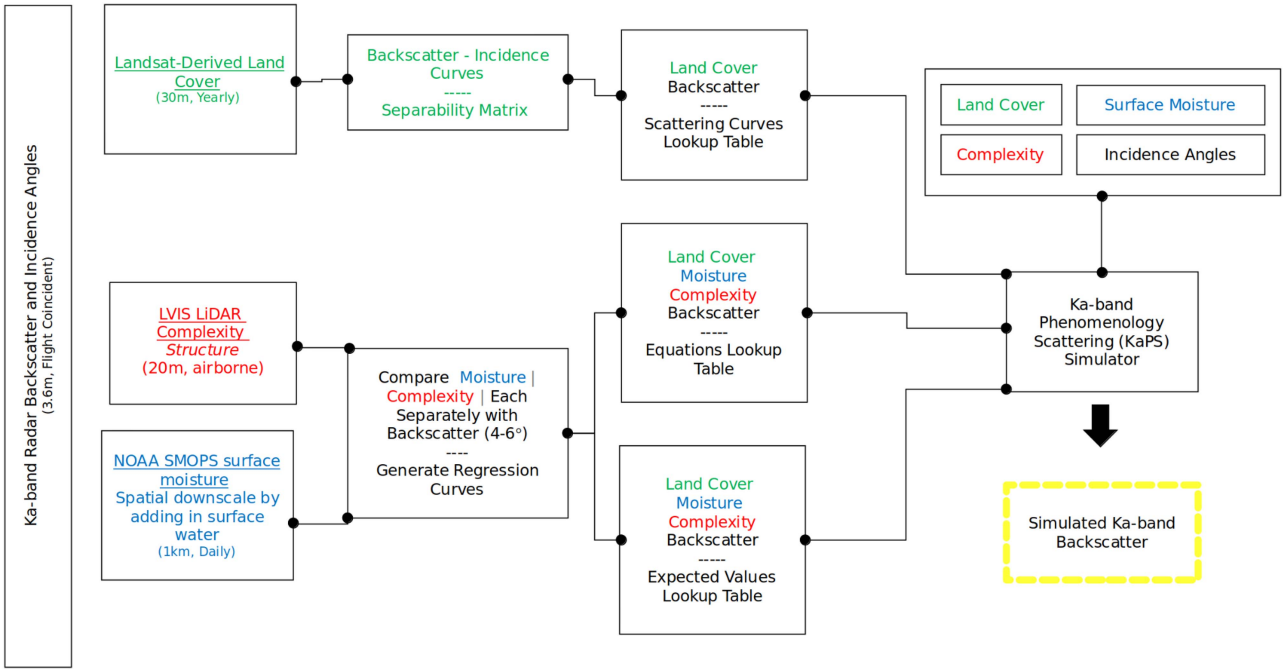

Fig. 2. Schematic diagram showing the stages of designing the KaPS model (first four columns) and producing a simulation. Reference land cover (green), moisture (blue), and complexity (red) data are preprocessed and compared with Ka-band radar backscatter to produce empirical scattering curves and look-up tables of parameter-backscatter relationships and expected values. The derived empirical scattering curves and look-up tables form the foundation of the KaPS Ka-band backscatter simulator.

vegetation, wet soils, and land vegetation are separable (i.e., distinguishable) in Ka-band backscatter imagery, the ADLC reference land cover dataset is compared with AirSWOT images as follows. First, the AirSWOT images are reprojected to the same coordinate reference system as the ADLC, and the AirSWOT pixels are converted to vector points to extract the land cover directly corresponding to each radar pixel using a nearest neighbor extraction. Next, the separability metric [69], [70]—a modification of the standard score, and defined as the difference between the linear backscatter means (μ) and standard deviations (σ) for each pair of land cover classes (class i and class j)—is used to calculate separability of land cover classes from each other in the AirSWOT data [Equation (1)]. Land cover class pairs with separability values greater than 2 are considered separable, or unlikely to be confused when classified. For each pair of land cover classes i and j and each 3° incidence angle bin k the separability metric S is calculated as

$$S_{i,j,k} = \frac{|\mu_{i,k} - \mu_{j,k}|}{\sigma_{i,k} + \sigma_{j,k}}. \tag{1}$$

Because this study focuses on identifying the occurrence of non-water observations being misclassified as water, the separability metric can be modified to refer to individual observations within the class to produce a percentage likelihood of misclassification. Here, the group of observations from one class (j), are compared with the means and standard deviations from the reference class (i) [excluding the standard deviation from class j, converted to 0 in (2)]

$$S_{i,j,k} = \frac{|\mu_{i,k} - Obs_{j,k}|}{\sigma_{i,k} + 0}. \tag{2}$$

As a result of this calculation, $S_{\mathrm{i,j,k}}$ has the same number of values as the input observations from the class (j), giving each observation its own separability value. For each class (j) the number of observations of the separability values greater than the reference separability threshold, 2, out of the total number of observations is assessed as the separability ratio. This equation allows us to determine the misclassification likelihood of water compared with other land types.

2) Influence of Surface Moisture on ka-Band Surface Scattering: To assess the influences of moisture on Ka-band backscatter, the NOAA SMOPS volumetric soil moisture percentage data are spatially downscaled to 1 km posting, to more closely approximate the spatial and temporal extent of AirSWOT acquisitions. The downscaling methods are summarized here and are explained in more detail in the appendix.

Prior to downscaling, each pixel of the 25 km volumetric soil moisture percentage data is five times the swath width of the AirSWOT flight lines, allowing only broad-scale comparisons of regional moisture variations. Over the vast AirSWOT study domain during a time of seasonal hydrologic change in the region [52], substantial changes in soil moisture are observed even in coarse resolution SMOPS data. The surface moisture data have a daily temporal resolution, sufficient for monitoring changing surface moisture for this purpose. However, SMOPS

omits inland water bodies, complicating the assessment of AirSWOT radar backscatter over open water. To mitigate this, water bodies from the 30 m ADLC dataset are merged with the 25 km SMOPS dataset to produce a 1 km, higher resolution product. As the moisture products are limited to the range of 0%–60%, and volumetric moisture content refers to the ratio of the volume of water to the unit volume of soil, adding water features increases the range to 100% for open water. The soil moisture downscaling produces products that visually show both the original 25 km large pixel shapes and ADLC water bodies. This final 1 km daily resolution downscaled product is called "surface moisture" rather than "soil moisture" because open water bodies are included. The spatial downscaling methodology is explained in more detail in the Appendix Section A, and Fig. 12.

3) Influence of Surface Structural Complexity on Ka-Band Surface Scattering: Radar backscatter varies with surface dielectric constant and geometry (assessed here in the form of volumetric moisture and LiDAR complexity) [71], [72]. Because the incidence angles assessed in this study are less than 30°, scattering is dominated by reflections from appropriately oriented facets on the surface [73]. In this case, leaves provide diverse orientations and the structure of the vegetated canopy provides a mixture of facets and gaps as demonstrated in Fig. 1. Because LVIS LiDAR is full-waveform, it is able to capture signal returns of different strata within the vegetative canopy, providing information on vegetation density diversity and, therefore, canopy structure. The LVIS LiDAR complexity metric measures the vertical heterogeneity of surface features and is related to the LAI [68]. These metrics are also related to two-way transmissivity, as less LVIS LiDAR energy is returned from dense, highly complex canopies than from sparse canopies and bare ground with low complexity. While the complexity metric does not directly provide any information regarding the orientation of the surface facets, leaves with horizontal rather than vertical orientations are more exposed to LiDAR pulses, which may have greater contributions to the assessment of counts per elevation bin. Thus, the relationship between LiDAR complexity and Ka-band scattering is hypothesized to be indicative of the two-way transmissivity of Ka-band, assuming a near-uniform distribution of leaf and branch orientations.

4) KaPS Model: A Simple Empirical Statistical Model to Simulate Near-Nadir and Low Incidence Ka-Band Surface Scattering: To simulate how Ka-band scattering may vary over space and time, the study develops a simple statistical scattering model based on near-nadir surface moisture and LiDAR complexity to estimate backscatter (see Fig. 2). To develop the model, the relationships between scattering (y) and each of these parameters (x_i = moisture or structural complexity) are investigated independently for binned backscatter values. It is important to note that the incidence angle range for this examination is limited to 4°–6° to reduce the incidence angle-driven scattering variability. This investigation is conducted by subsetting the data into 15 ADLC land cover types and correlating each of the two parameters with backscatter. The two parameters are examined separately to identify the strength of the relationship for each parameter alone and to support inverse modeling; land covers are examined separately because various land covers are expected to have different scattering mechanisms due to differences explained by moisture and complexity (geometry). Following the investigation of the two scattering parameters, nonlinear equations describing these relationships are used as the framework for the model. Two formulas (for each x_i = moisture or structural complexity) are generated for each land cover type, estimated first using a loess local regression to reduce the influence of outliers prior to estimating the nonlinear relationships.

For each land cover, observed backscatter values from pixels with incidence angles between 4° and 6° are binned into ∼0.5 dB groups to extract the mean and standard deviation for each parameter, creating a look-up table of expected values for each backscatter bin. Next, scatterplots and nonlinear equations of these expected values are produced for each parameter and each land cover. While backscatter may be estimated using each of the equations separately, it is expected that the variable importance of each parameter will not be the same for each land cover type and therefore none of the two parameters should be used alone to estimate backscatter. A single equation for each land cover is produced with weighted contributions from each parameter. Weights are assessed to maximize the coefficient of determination (R^2) when the weighted averaged estimates are compared with the binned observations. The direct output of the combined regression formulas is applicable to the reference incidence angle range 4°–6°, but estimates of higher incidence backscattering can be produced by using the 4°–6° reference value (for pixels within and outside of this incidence range), modulated by the quantile scattering curves for higher incidence angles. Finally, 2-D density plots (backscatter versus parameter, unbinned) are used to estimate the probability that the estimated value will occur. A secondary map depicting backscatter confidence may be produced alongside the backscatter map using these probability plots. Together, the pair comprise the KaPS model. A flow chart demonstrating this framework is shown in Fig. 2.

III. Results

1) Separability of Near-Nadir and Low-Incidence Ka-Band SAR Backscatter for Wet Surfaces and Diverse Land Covers

Open water and dry vegetation are typically distinguishable in the AirSWOT data. Backscatter values extracted from the ADLC demonstrate variation in scattering for different land cover types for incidence angles 2° to 27° (see Fig. 3). For dry land classes, the average backscatter for incidence angles less than 5° is often very low (∼0 dB), with a small standard deviation across the 2° to 27° incidence range, compared to wetter surfaces. The open water class shows consistently high scattering at small incidence angles (∼15 dB at 3°), and sharply decreasing backscatter with increasing incidence angles, as expected from the smooth surface. The shallow-littoral zone of water bodies contains both water and emergent or floating vegetation, producing bright scattering as indicative of the smooth scattering source of the underlying water surface and perhaps

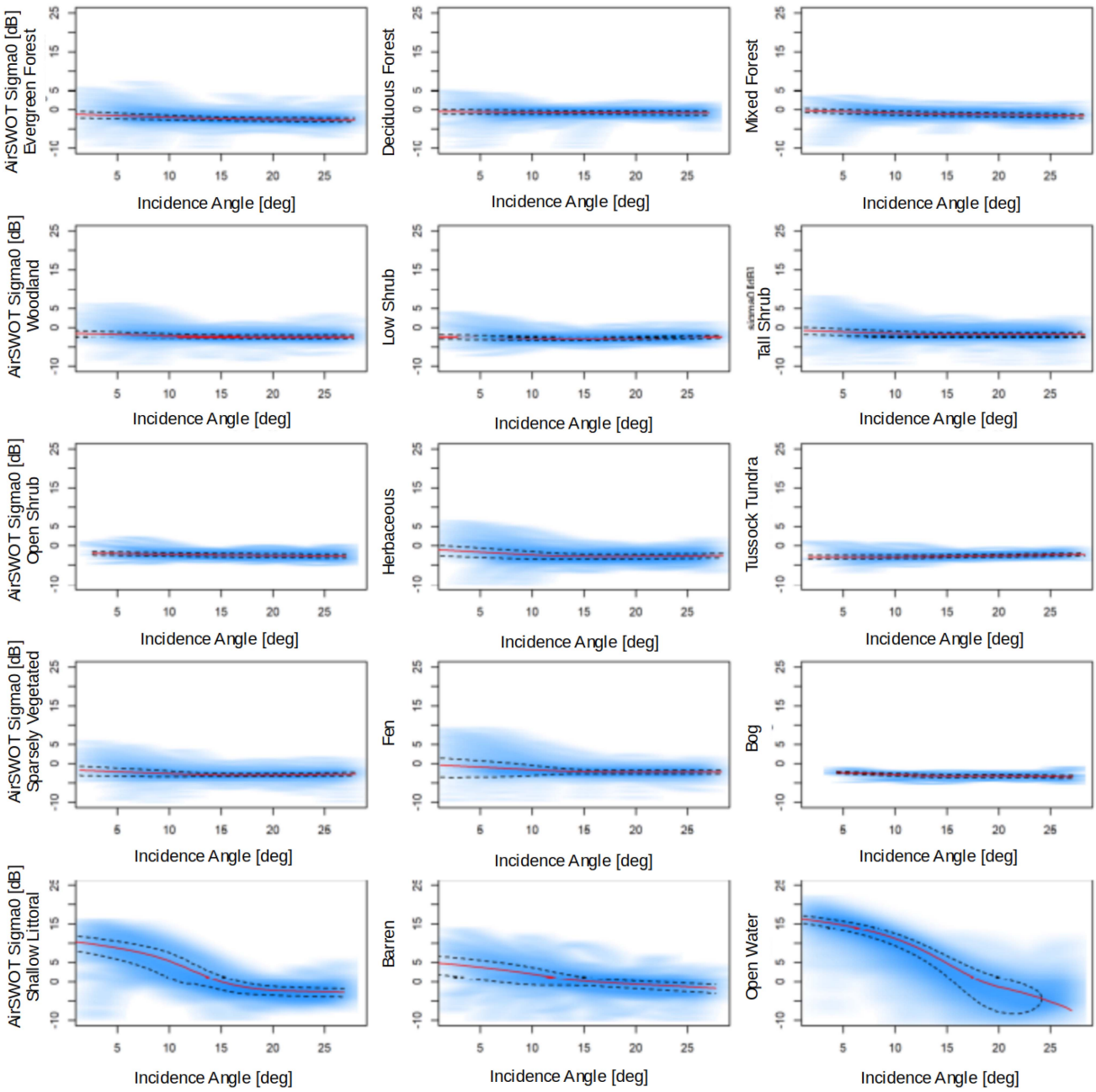

Fig. 3. Extracted Ka-band backscatter from 2017 AirSWOT 2017 flights acquired over the ABoVE domain. The red line shows the average backscatter, while the black dotted lines present the 32nd and 68th percentiles around the average. The blue shading shows the 2-D density of the observations, excluding outliers. The majority of land covers have low backscatter across all incidence angles, while wetter surfaces such as water and littoral zones have higher backscatter at lower incidence angles. The barren class shows a higher standard deviation, particularly at the near range, demonstrating more variability.

some double-bounce scattering [74]—observed as bright rings around some small lakes with reedy vegetation—between the vegetation and the water surface (∼7 dB at 3°). The barren land cover shows brighter backscatter than vegetated dry land (∼3 dB at 3°). Bright scattering from barren land surfaces is indicative of the variability in the land cover itself. While barren surfaces are not generally considered to be specular, they may be very flat, smooth, and planar; they may also be wet, having similar scattering as the littoral zone vegetation or the open water in some cases. It is also important to note that there is significant within-water class variability, primarily due to wind-driven surface waves [41], which can increase the backscattering over water by up to 15 dB with increasing wind speeds [75].

For all observed dry-land cover classes, there are few bright pixels at small incidence angles (<5°). The low occurrence of bright scatterers for vegetated land cover classes demonstrates that it is uncommon for these classes to be very bright in these Ka-band observations, limiting their impact. These anomalously high backscatter returns from the vegetated classes are likely to be caused by differences in resolution and misclassification,

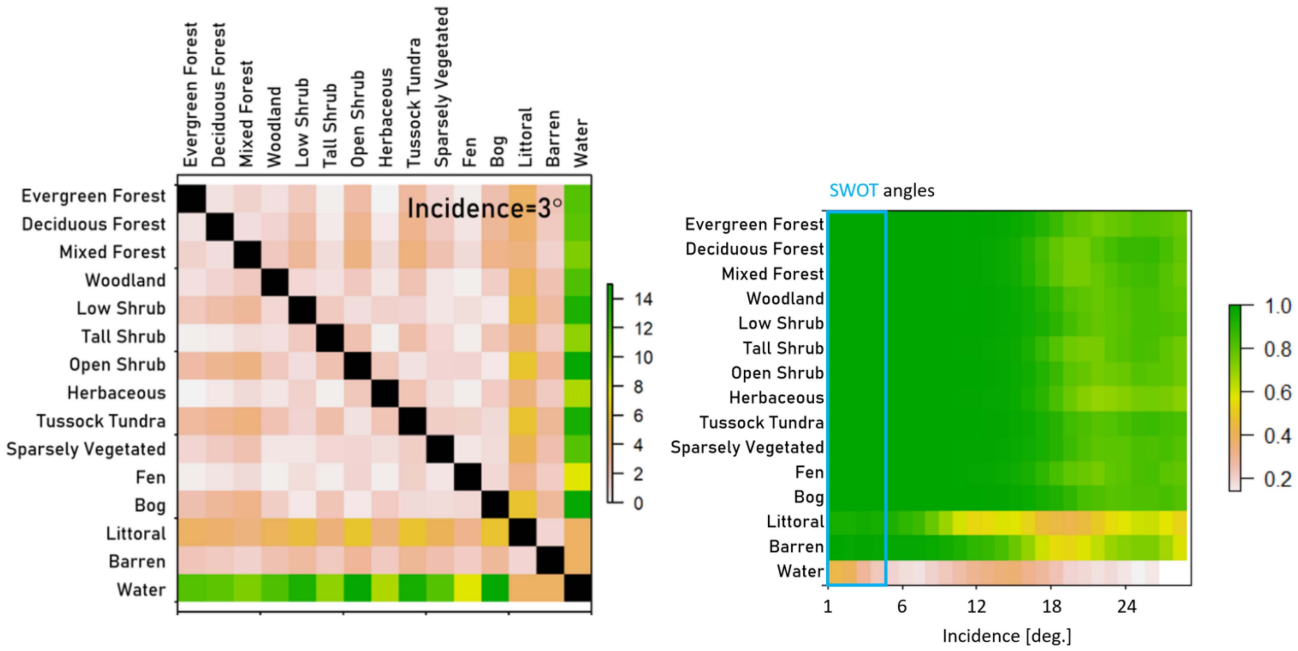

Fig. 4 Left. The separability metric (1) is calculated for each land cover class combination for the 0°–3° of incidence bin to determine the separability between each pair of land cover classes. Pairs of classes with values greater than 2 are considered separable. Fig. 13 (appendix) segments and highlights values greater than 2 in a binary image. Right. The modified separability metric (2) is applied to each land cover class in contrast to the open water class, along all incidence angles, to identify how separability changes as a function of incidence angle. Open water is shown to not be separable from itself as expected, and many land cover classes are shown to be consistently separable from water. For near-nadir SWOT-like incidence angles, and low incidence angles up to 15°, open water is considered to be highly separable and distinct from other classes.

as a few bright scatterers classified as vegetation in the ADLC were found to be small water bodies or built-up regions observed from the AirSWOT optical camera data. In addition, pixels from other surface classes, such as water or littoral zones, may be included in the extraction of a similar short vegetation class due to uncertainties in the land cover classification.

At incidence angles around 5°, water differs from all of the vegetated land covers (see Fig. 3). However, the differences between water, littoral zone, and barren soils are smaller, though they are still distinguishable on average in Fig. 3.

By applying the separability metric [69], the study quantifies to what extent the scattering is similar or separable for each land cover class and incidence angle (see Fig. 3). The separability metric takes into account the variations in the surface scattering of the water, making it comparable to land, given different amounts of water scattering.

The separability matrices shown in Fig. 4 demonstrate that open water is highly separable from most land cover classes from low SWOT-like incidence angles up to mid-range AirSWOT incidence angles ($\sim 3 \lesssim 12°$). As separability values greater than 2 are considered highly separable or distinct classes [70], the open water separability values of 5–15 compared with all other classes demonstrate that water is highly distinct. Fig. 13 (appendix) demonstrates a thresholded metric, highlighting values greater than 2. Excluding the littoral zone and barren classes, the separability of other land classes is even higher (8–15), demonstrating that open water has up to five times greater separability compared with vegetated land cover classes and is twice as separable as littoral and barren classes. Since the separability metric measures the distances between classes through the mean and standard deviation values, separability refers to only one standard deviation of observations and therefore represents the majority of cases but not all cases.

The majority of the time, open water, littoral zone, and barren surface classes are separable from each other, which is the ideal scenario for SWOT and for future applications of Ka-band data. However, under certain conditions, the differences between these three classes narrow, particularly when non-water classes exhibit higher than expected backscatter, such as with urban regions (i.e., CNES press release example over Toulouse, France), which were outside the scope of this study due to lack of observations, or when vegetation becomes flooded, causing a bright double-bounce phenomenon. These results are corroborated by similar studies looking at more coarse-resolution GPM data [29], [63]. These findings suggest that it is additionally important to assess the influence of changing surface conditions, which may cause changes in backscatter.

2) *Influence of Surface Moisture on Ka-Band Surface Scattering*

To assess the relationship between backscatter and moisture, the moisture products were spatially downscaled to 1 km for comparison AirSWOT observations. The results of the downscaling for moisture are shown in Appendix Fig. 1. For information on how moisture, temperature, and backscatter covary, see previous work [28].

A strong correlation between surface moisture and backscatter is shown in Fig. 5. Using 0.5 dB backscatter bins, the mean and standard deviation moisture values are assessed for each bin

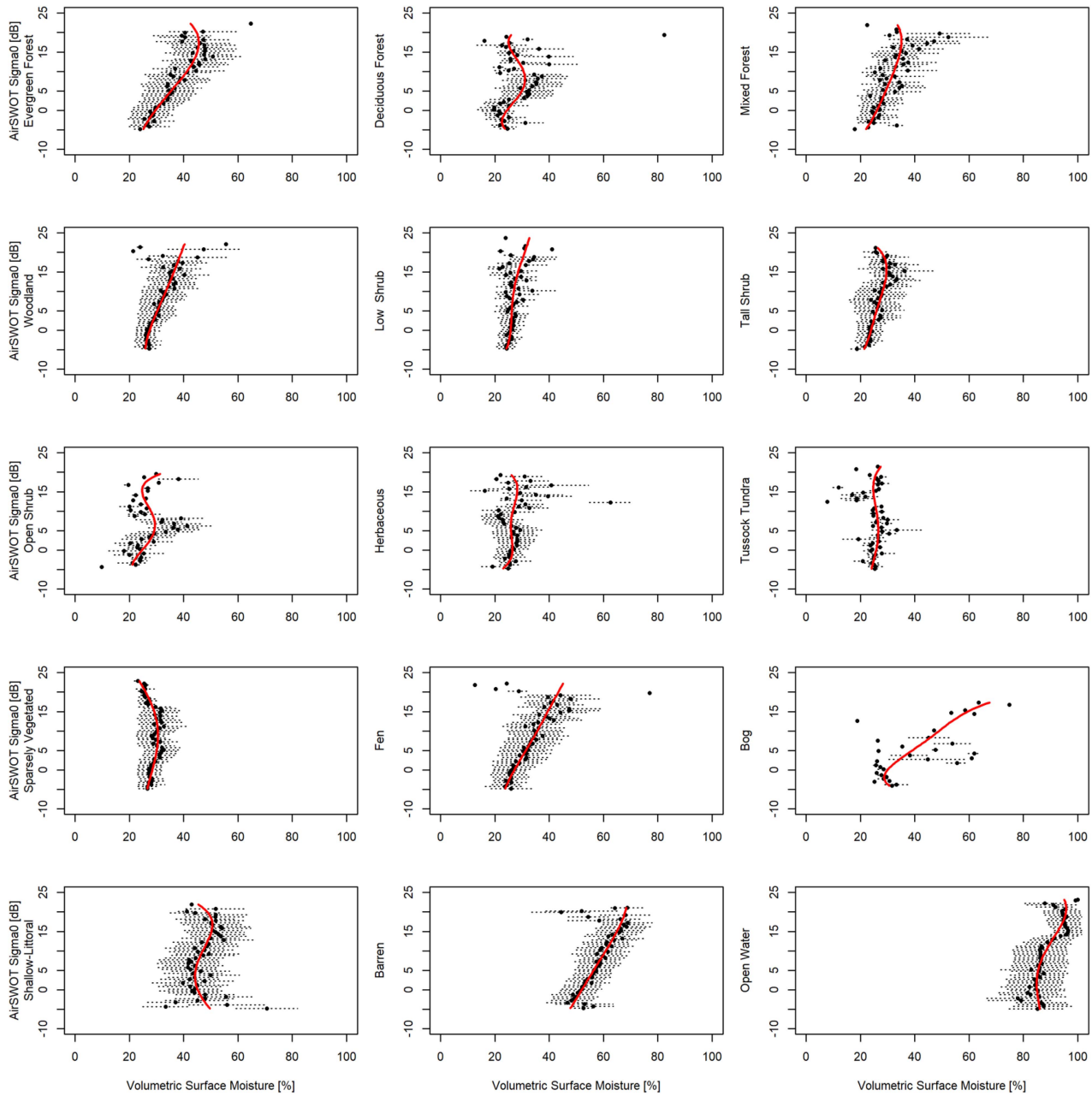

Fig. 5. Mean (black dots) and half-standard-deviation (horizontal lines) surface moisture values assessed for each 0.5 dB bin for each specific land cover, limited to 4°–6° of incidence. Littoral zone, barren soils, and water have the highest surface moisture of the 15 classes. For each land class, a best-fit regression (red curve) yields an empirical backscatter-moisture relationship unique to each land cover.

and for each land cover. Bins are limited to incidence angles 4°–6° to limit the incidence angle-related change in backscatter. Most land cover values have low moisture, as expected, with the exception of the three classes of interest: littoral zone, barren soils, and water. A polynomial regression curve (red curve) is drawn through the mean values for each of the land cover classes, producing backscatter-moisture relationships that are unique to each land cover.

The variation between the moisture values of the land cover classes presented in Fig. 5 can be explained as follows. The shallow-water-littoral zone contains a mixture of vegetation and water; however, the surface moisture data is limited by the spatial resolution of the data and the artificial addition of moisture for wet areas such as open water bodies, which was not possible with the littoral zone. Thus, the mixture of water and vegetation would provide an expected observed surface moisture value ranging between 30% and 50%. The barren surface classification sometimes consists of exposed soils of rivers and lake beds on the edge of water bodies. Across the ABoVE domain, where the land cover data was produced, there is also an abundance of exposed rock and bedrock, particularly closer to the Canadian Shield in the east. However, the areas that are examined here rarely include these rocky surfaces, and therefore dry, barren surfaces have fewer occurrences in this analysis compared to near-water

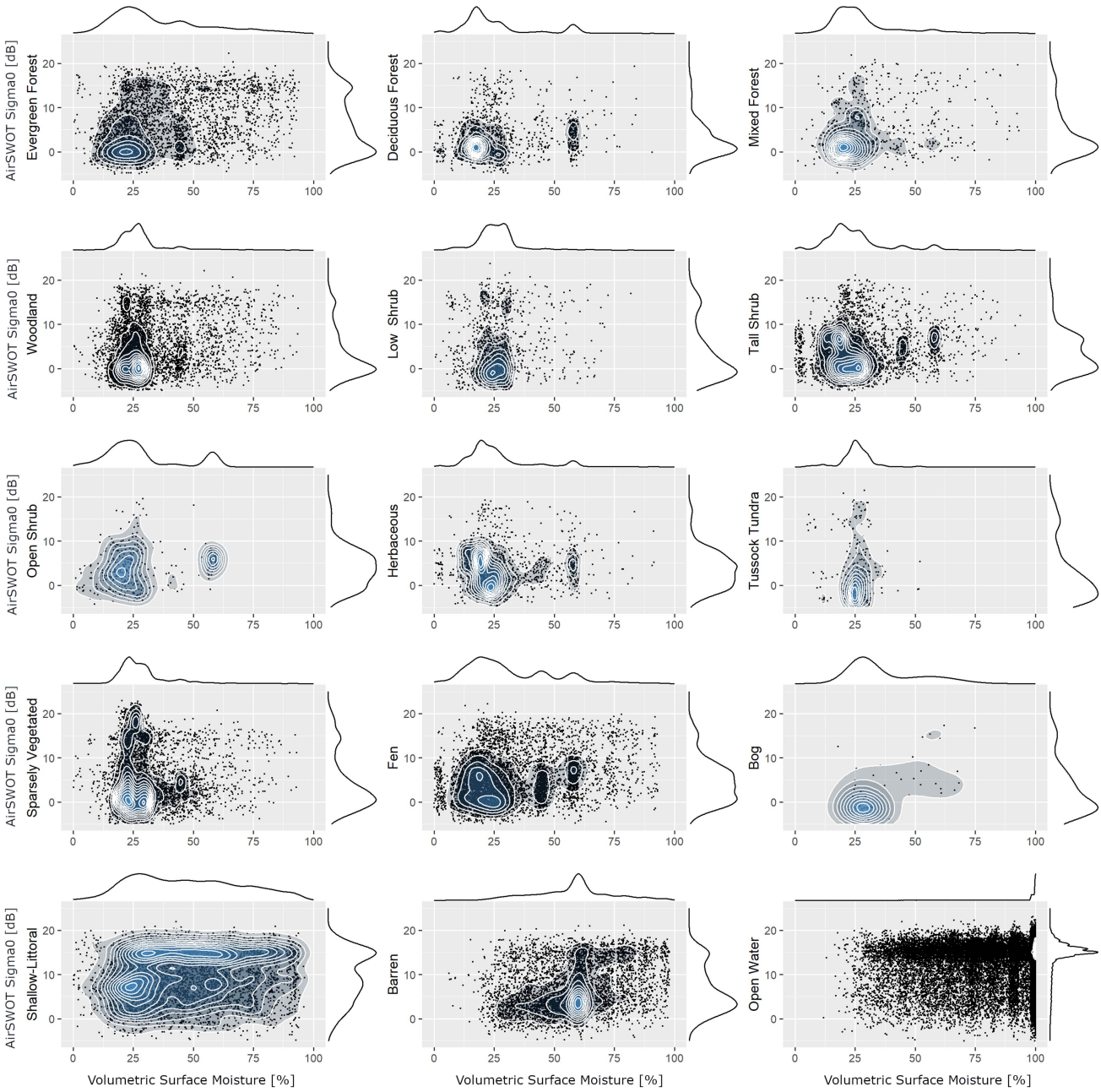

Fig. 6. Scatterplot of the backscatter- moisture observations are shown for each land cover type, different from the binned plots above, for incidence angles 4°–6°. Blue contours show dense clusters of points, supported by probability density lines on the *x*- and *y*-axes, revealing probable scattering values. These figures demonstrate the likelihood that a given backscatter value or moisture value would be observed, given the seasonal observation range of July–August 2017.

soils or exposed lakebeds, leading to a wetter moisture range of 40%–65%. Finally, open water has a range of 80%–100% moisture, explainable by the differences in spatial resolutions between the ADLC, surface moisture, and radar data products. The large standard deviations of moisture within each bin and high slopes of the fit lines suggest that the accuracy of the backscatter estimate from moisture alone is limited.

While the regression curves are designed to show the expected backscatter value given a specific surface moisture value based on the trend, any specific combination of moisture and backscatter may or may not be statistically likely to occur. For example, it was previously noted here that some mixed water-land pixels would have a lower moisture value and less backscatter. It is thus ideal to understand the expected backscatter of mixed pixels; however, across the observations, mixed water pixels are not particularly likely. Fig. 6 shows the unbinned observations as a 2-D density plot highlighting the backscatter-moisture pairs that are particularly likely.

As previously mentioned, the open water class may become mixed water along the edges of channels and lakes, lowering

the scattering value, although this is not particularly likely for areas that are classified as open water. However, the littoral zone, which is a transition between open lake water and land, represents a very large range of expected moisture values, which also explains why the alignment of the mean values from this class represented in Fig. 5 is vertical. The littoral zone cover class shows that backscatter can be high even when the ground is not particularly wet, supporting the idea of mixed pixels and an imprecise moisture reference, and additionally raises the idea of backscatter variability based on surface texture and geometry at different vertical scales. Unlike dense forest types, the littoral zone contains thin, non-woody vegetation varying vertically up to three meters, which would allow Ka-band penetration or transmission, producing backscatter from different heights. Moisture variability cannot fully describe the variability of the Ka-band backscatter, possibly due to these surface complexities over varying vegetation types. To begin to answer these questions, the next section examines surface and vegetation structural complexity through the lens of LiDAR observations coincident with the Ka-band observations.

3) *Influence of Surface Structural Complexity on Ka-Band Surface Scattering*

Full-waveform LiDAR data from the LVIS provide information on surface and vegetation structure. Low complexity values (close to 0) are usually flat ground or water surfaces, while higher complexity values (close to 1) are usually dense canopies. In practice, for this region, complexity values rarely exceed 0.6, with the exception of infrequent measurement errors, easily recognizable as a stripe through the center of the flight segment. These errors appear to be more apparent over water bodies, and so for the purposes of this analysis, all complexity values greater than 0.6 are omitted.

Using the same method of comparison as with the moisture data, backscatter values are binned into 0.5 dB groups (y-axis) and the average (points) and half-standard deviation (lines) of the LVIS complexity values are plotted on the x-axis. All land cover classes have at least some observations of low complexity due to land cover variability, misclassification, and diverse densities of land covers. High complexity values are typically found in forest and shrub classes. Forest and shrub vegetation classes show higher backscatter in low complexity areas and relatively lower backscatter when complexity increases. Because complexity is a measure of vertical structure and density, the decreased backscatter signal is indicative of the decreasing radar and LiDAR transmittance through thicker canopies, producing "L" and "C"–shaped backscatter-complexity relationships. However, it is important to note that the shapes are not uniform across the different land cover types. This is important because it indicates that the Ka-band backscatter is sensitive not just to surface complexities, but also to foliage type, as the Evergreen Forest and Deciduous Forest classes have very different scattering curves, for example.

Though the data in Fig. 7 represents the scattering relationship between LiDAR complexity and Ka-band backscatter using backscatter bins, very low backscatter values in the case of water, and very high backscatter values in the case of dry land, are not particularly common. The purpose of Fig. 7 (and Fig. 5) is to demonstrate the contributions of backscatter variability if a given backscatter value is observed. Fig. 8 demonstrates the probability that a land cover type will have a high or low complexity value.

Likely backscatter values are estimated for dry land using the frequency distributions and backscatter–complexity relationships (see Figs. 7 and 8). Combining complexity-based estimates with moisture-based estimates accounts for dominant factors in scattering variability across the landscape. Building this simple model enables the production of backscatter simulations sensitive to changes in moisture and surface complexities, as described next.

4) *KaPS Model: A Simple Empirical Statistical Model to Simulate Near-Nadir and Low-Incidence Ka-Band Surface Scattering*

This study introduces a simple empirical statistical model for near-nadir and low-incidence Ka-band surface scattering, called the KaPS model, to demonstrate likely variations in surface scattering due to diverse and changing moisture conditions and land covers. The KaPS model weights and averages the two output backscatter estimates from the complexity-backscatter and moisture-backscatter equations, and modulates the backscatter value given the simulated incidence angle. When both data sources—moisture and complexity—are available, the data can be input directly into the model. When data is unavailable, a look-up table, supported by frequency distributions (see Figs. 6 and 8) can be used to estimate likely values based on land cover type. KaPS initially produces a backscatter estimate for a given pixel based on the moisture and complexity values. The backscatter values from each equation are combined using an iterative weighting technique to maximize the R^2 when compared against the observed, randomly sampled, and binned AirSWOT data. These values are only applicable for the reference incidence range (4°–6°) and can be used as a reference for higher incidence angles extending to 27° using quantile curves extracted from the land cover-backscatter-incidence angle relationships. For the 4°–6° incidence angle range, Fig. 9 demonstrates the relationship between the estimated backscatter values produced from KaPS, and the original binned backscatter values from AirSWOT. Note that the KaPS estimated backscatter values were generated from the regression equations assessed at previous steps; the data used to produce the regression equations includes 50% of the data, randomly sampled. Because the data is binned and aggregated, there is no significant difference when sampling 30% or 70% of the data. The mean and median R^2 from the KaPS and AirSWOT comparison "best case" across the 15 surfaces are 0.74 and 0.72, respectively; the mean and median RMSE are 3.5 dB and 3.9 dB; the mean and median MAE are 2.7 dB and 3.22 dB, demonstrating that the majority of the backscatter variability is captured by moisture and LiDAR complexity, while the remainder of the variability is likely due to finer, wavelength-scale roughness features ($\sim$1 mm, a fraction of the 8 mm wavelength), and topographic influences to the land cover, which are not examined in this study.

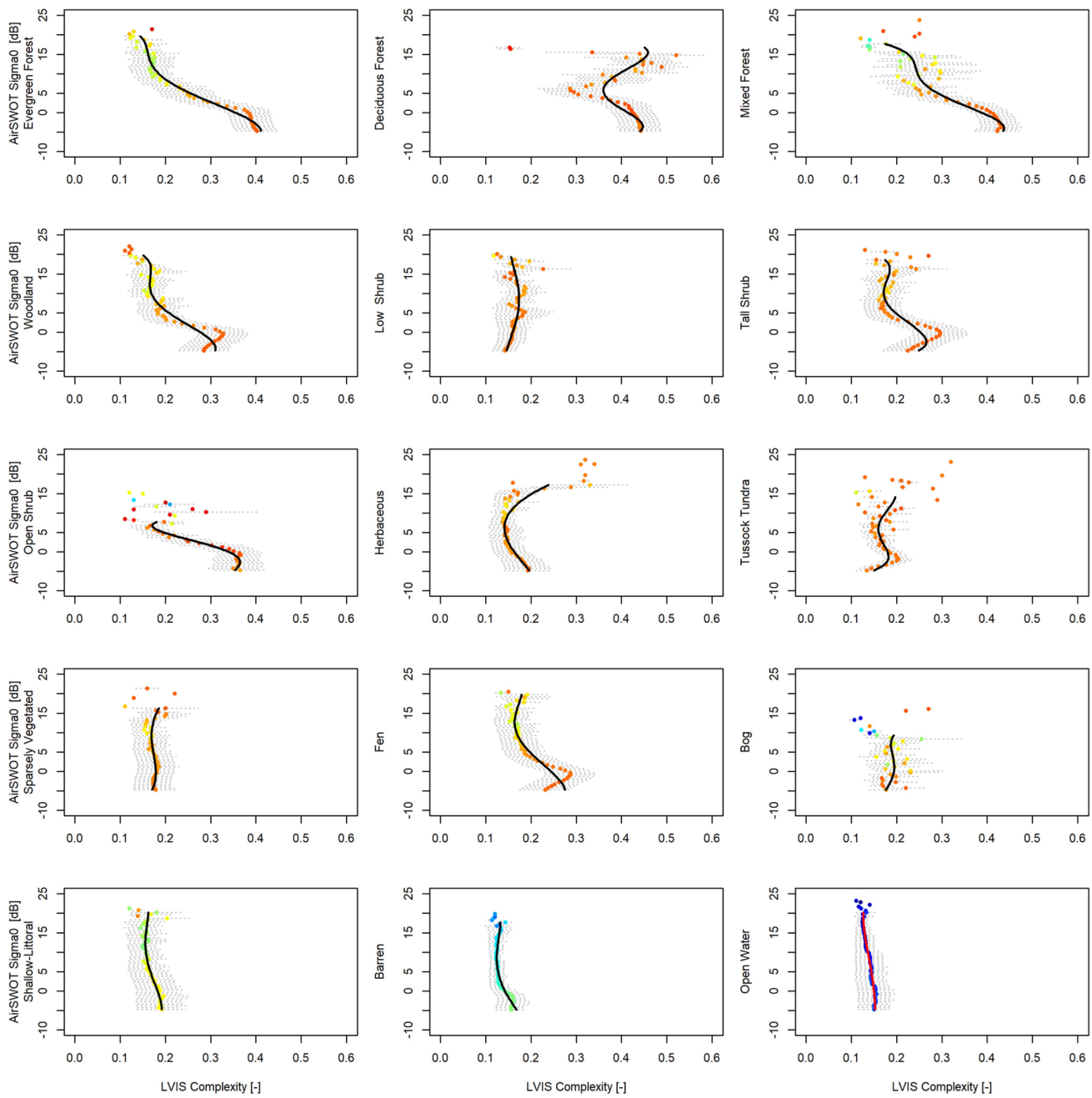

Fig. 7. Mean (dots) and half-standard-deviation (horizontal lines) LVIS LiDAR complexity values assessed for each 0.5 dB bin for each specific land cover, limited to 4°–6° of incidence. Colored dots represent moisture where blue dots are very wet and red dots are very dry. Forest and shrub vegetation classes show a decreasing trend of backscatter with increasing complexity, whereas other land cover classes, such as water are limited in their complexity variability. For each land class, a best-fit regression (black curve) yields an empirical backscatter–complexity relationship for that class.

Three look-up tables are used to simulate backscatter.

1) Incidence Angle—Backscatter Quantile Curves (see Fig. 3; see also Appendix Table I), and
2) Formulas with weights for the LiDAR complexity and moisture components and the resultant "best case" R^2 value (see Appendix Tables II–III), and
3) Expected values and probabilities for moisture, LiDAR complexity, and backscatter as seen in Figs. 5–8 (see Appendix Table IV).

To simulate the backscatter from a given surface, either surface complexity, surface moisture, or both are required as inputs alongside a map of incidence angles for the coverage area. Given input reference data and an incidence angle map (as in the example shown in Fig. 10), the workflow is as follows. If both complexity and moisture datasets are available, the near range (4°–6°) reference backscatter values may be computed directly. If one or the other dataset is unavailable, the available data value for each pixel can be used as a starting point in the

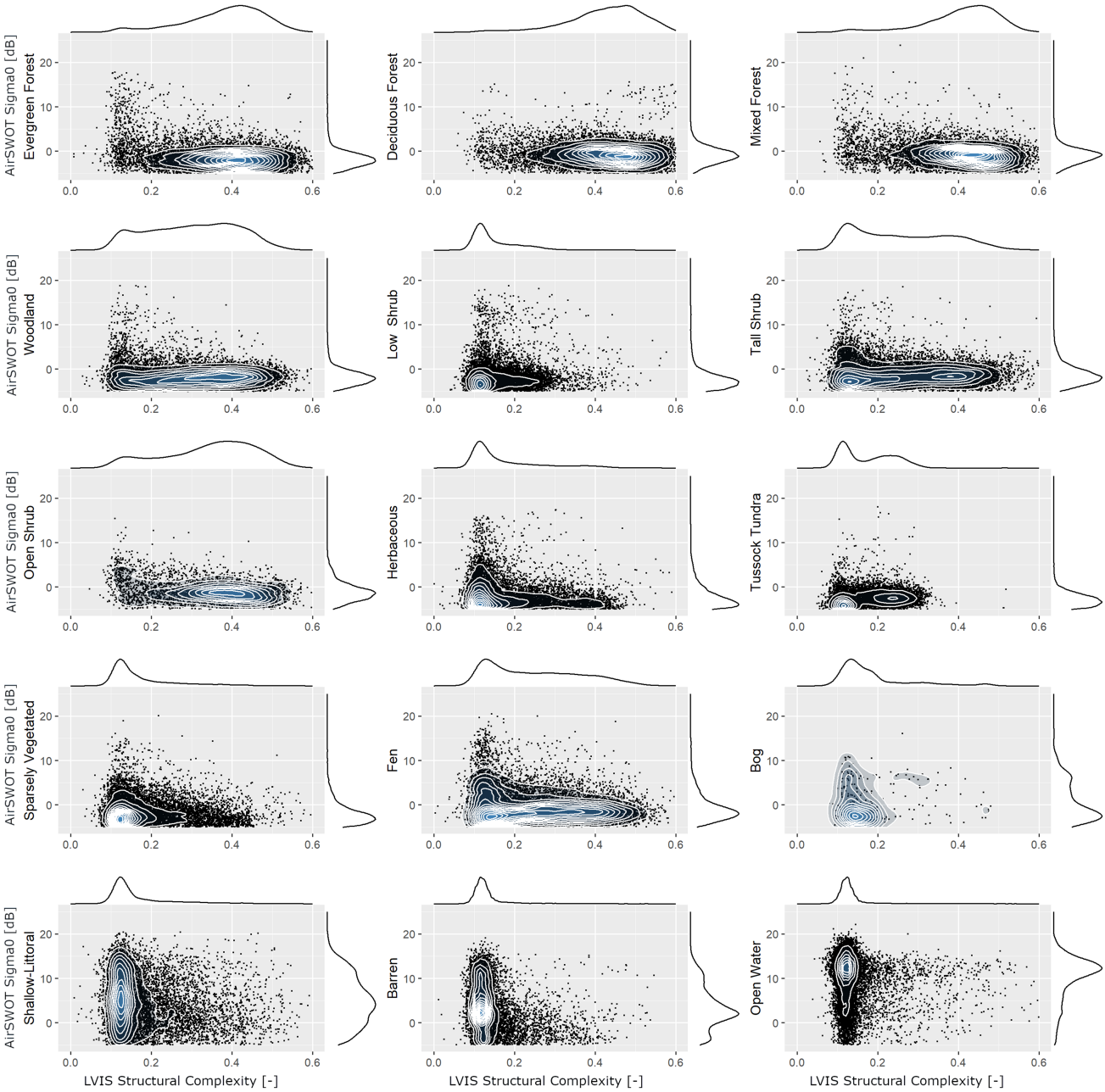

Fig. 8. Scatterplot of the backscatter-LVIS LiDAR complexity observations are shown for each land cover type, different from the binned plots above, for incidence angles 4°–6°. Blue contours show dense clusters of points, supported by probability density lines on the *x*- and *y*-axes, revealing probable scattering values. These figures demonstrate the likelihood that a given backscatter value or complexity value would be observed, given the observations from July 2017.

Expected Values lookup table (Appendix Table IV), pointing to the likely value for the other dataset. Given the observed value from one dataset, and an estimated value selected from the lookup table, the values can be manually input into their corresponding equations. Finally, if neither value is known, KaPS can be used to simulate the backscatter response from generated surface complexity and moisture maps or manually coded values.

KaPS demonstrates possible radar backscattering values for wet and dry earth surfaces. KaPS simulations show good visual agreement with water bodies, wet vegetation, and soils as compared with AirSWOT observed Ka-band radar backscatter data (see Figs. 9 and 10). KaPS additionally highlights the sensitivity of radar backscatter to surface moisture, as the increased moisture jump from the low-resolution 25 km SMOPS tile, from ∼30% to 60% moisture, results in a dramatic increase in radar backscatter (see Fig. 10). Soil moisture is generally accepted to be saturated at around 50%–60%, where backscatter increases with increasing moisture until the surface is saturated. KaPS model output in Figs. 10(f) and 11(b)demonstrates this

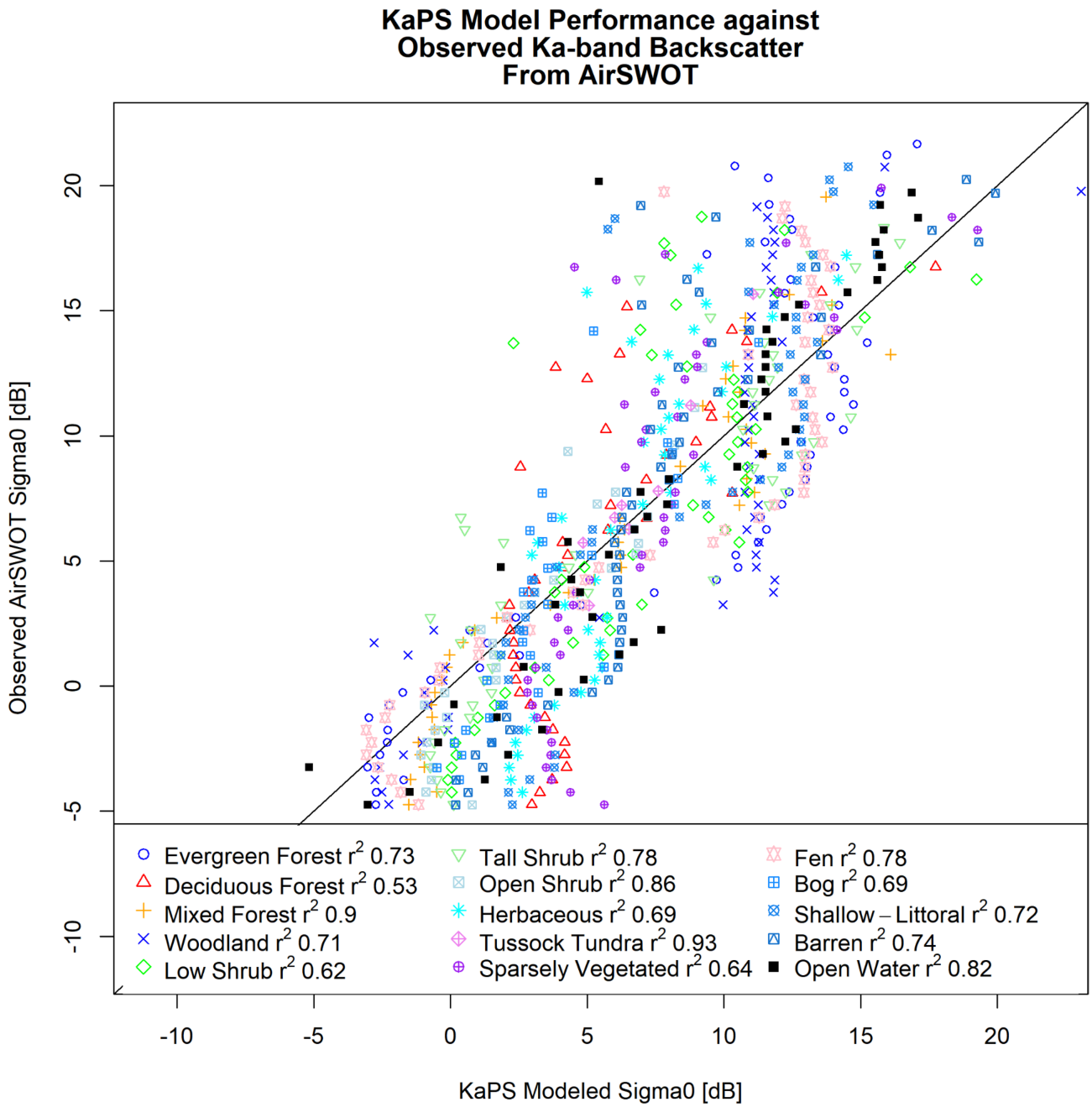

Fig. 9. Binned backscatter observations from AirSWOT versus simulated or "expected" values from KaPS. Backscatter values are simulated for each land cover independently based on AirSWOT-derived empirical relationships between moisture, surface complexity, and backscatter. These estimated values represent a "best case scenario" for how closely the data can be estimated. As these values are based on broad-scaled binned observations across the whole region, they do not correspond to expected spatial correlations or variability at the local scale, as these values will depend on the resolution and accuracy of the input data.

sensitivity as brighter backscatter cutting diagonally across the center of the flight line, corresponding to higher moisture from the reference data. Following the available data from the reference products, because the LVIS data have an irregular shape and a narrower swath width (∼1.8 km) compared to the AirSWOT data (∼3.2 km), the output KaPS simulation is limited to the same swath width as the LVIS reference. A zoom-in of the simulated output in comparison with the AirSWOT observations is shown in Fig. 11.

Simulating moisture and complexity variability by increasing or decreasing variables by 0%, 10%, or 20% provides a framework for predicting how the scattering will change when the surface changes—such as during deforestation (decrease in complexity) or during a flood (increase in moisture). Though the model, like most, is limited by the accuracy and resolution of the input data, the simulated outputs show good spatial agreement with the observed values, with low MAE (under 3 dB) for all 25 out of 25 simulations and RMSE (under 3 dB) for 16 out of 25 simulations, though the R^2 values are quite low (under 0.3), as expected, given the high-spatial resolution of the observations. Drying simulations (decreasing moisture by 20 or 10%) had lower RMSE and MAE values than the wetting simulations,

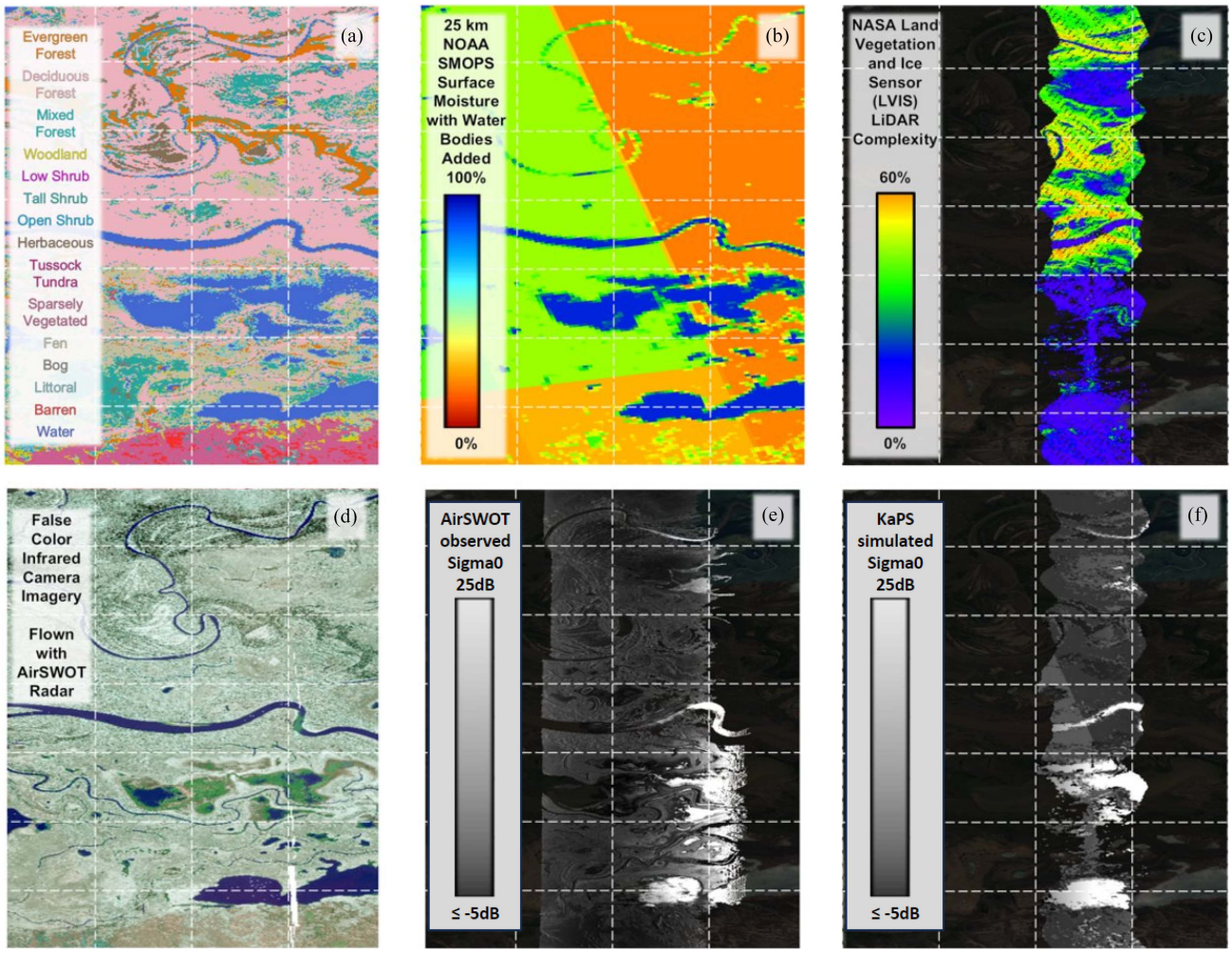

Fig. 10. Reference data and KaPS model simulation output for a transect through the peace athabasca delta (PAD) region, located in Canada (approximately 58.369N, 111.347W) with (a) Landsat-derived land cover ADLC (Wang et al. 2019), (b) NOAA SMOPS surface moisture, modified with added surface water for this study, (c) NASA LVIS LiDAR Complexity, (d) false color infrared image, collected simultaneously from the same aircraft as the AirSWOT Radar observations, (e) AirSWOT Ka-band backscatter, and (f) KaPS model simulation developed in this study. Note that the simulated backscatter (f) shows a diagonal line of brighter scattering in the center of the flight line as a result of increased moisture; the near-saturated moisture for that area is shown as a large green tile in the reference NOAA SMOPS data. As the KaPS model relies on the input data extents, the output KaPS simulation takes on the same irregular swath shape of the LVIS LiDAR complexity image and does not cover the full AirSWOT swath. If KaPS is applied to an area with a wider LiDAR extent (matching AirSWOT), the output would have more similar coverage to the original AirSWOT data.

emphasizing the importance of spatial variability and accuracy of the input moisture and complexity data. The complete table of the comparisons between the observed and simulated data is included in the appendix, Table V.

The KaPS model can be applied to any region having reference land cover and moisture datasets. As its purpose is to approximate near-nadir and low-incidence Ka-band backscatter, either modeled or remotely sensed data products may be used as inputs. In addition, moisture, surface structural complexity, and land cover may be varied within the model itself or by simply using different input data. The primary purpose is to be able to map water and land surface backscatter dynamics due to transient events (like moisture), with the expectation that relatively stable spatial differences due to heterogeneous surface complexity should be considered in order to assess the transient state of the surface. As observations of Ka-band backscatter are limited in temporal and spatial coverage, KaPS provides a method for creating simulated images of unobserved surfaces and estimating backscatter changes for those surfaces by including dynamic parameters such as surface complexity and moisture. Further, KaPS has the potential to be used for inverse problems, where backscatter values can be used to assess vegetation characteristics and surface moisture variability, although more work is necessary to demonstrate and prove the validity of the inverse case. Additional research is necessary and ongoing to identify sufficient model output and to calibrate and validate the KaPS model to be applied in the inverse cases. As SWOT was launched in December 2022, data is anticipated to become publicly available as early as October 2023, providing an opportunity to conduct these examinations with many more diverse conditions. Preliminary images from the CNES press release demonstrate that the KaPS model could

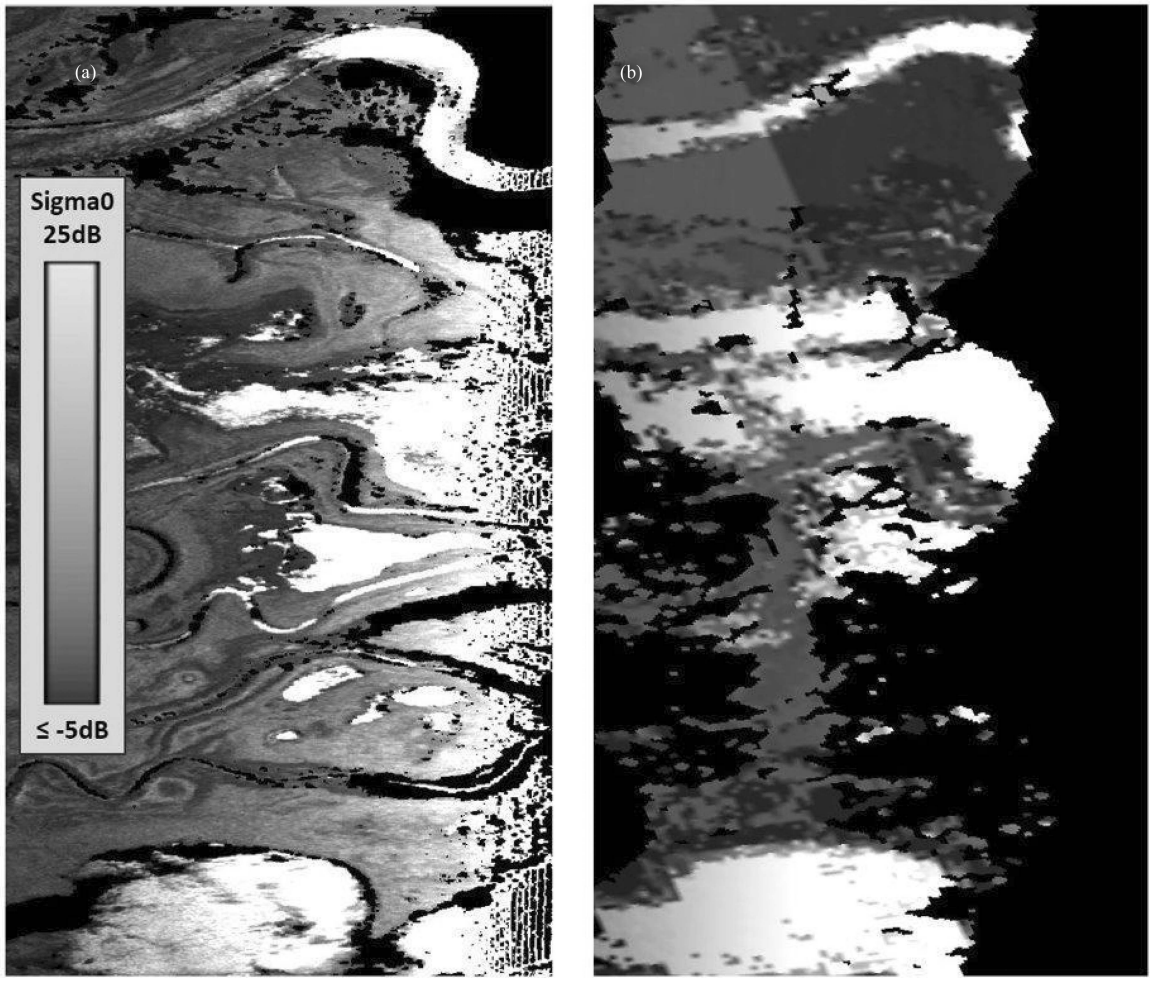

Fig. 11. Zoom-in of the simulated backscatter image [from Fig. 10(e) and (f)], containing river, lake, and wetland features. The simulation demonstrates an accurate presentation of these coarse-scale features, albeit limited by the input resolution of the reference moisture and complexity data. The AirSWOT observation (a), has a 3.6 m spatial resolution, while the KaPS simulation (b) uses input data with resolutions ranging from 20 m to 25 km. The KaPS simulation (b) uses LVIS LiDAR data, which has missing data, thus the simulated output correspondingly has missing data in the same location.

be highly useful for understanding the backscatter variability over land features.

IV. Discussion and Conclusion

Near-nadir and low-incidence Ka-band scattering sensitivities are examined for diverse Arctic-Boreal land and water surfaces by segmenting NASA ABoVE AirSWOT observations by land cover and comparing observed backscatter values to remotely sensed moisture and structural complexity. Following this analysis, the study enabled the development of a statistical scattering model, KaPS, to simulate Ka-band surface scattering at near-nadir and low incidence angles for diverse land cover and moisture conditions.

This research quantifies observed Ka-band backscatter from wet soils considering both vegetation vertical complexity and moisture content. Moisture, a dominant component of the dielectric constant, is a well-known control on radar backscatter [71], although this has not historically been studied as extensively for higher frequencies, including Ka-band. In addition, the specularity or smoothness of various features has been under-examined for Ka-band backscatter from various terrestrial surface types, further limiting the knowledge about the occurrence of brightly scattering, non-water features. To gain insight into land surface variations through the perspective of the Ka-band frequency, airborne Ka-band observations are used to identify backscatter sensitivities to variations in land cover, moisture, and structure.

Ka-band radar backscatter-incidence angle curves from AirSWOT outer-swath data (see Fig. 3) demonstrate clear separation between water surfaces and dry vegetation. Using the separability metric [69], [70], open water is highly separable from all other land cover classes based on the minimum value necessary to consider groups distinct (five times more separable than land and two times more separable than littoral zone and barren soils) (see Fig. 4). Using the modified separability metric, observations of barren soil/sand bars and littoral zone vegetation are found to be confused with open water about 5% of the time, showing that it is sometimes possible for barren soils and littoral zone vegetation to produce backscatter values similar to open water.

The observed backscatter is strongly dependent on moisture, evidenced by the high moisture variability across the

spatial domain and the seasonal water level dynamics. Without distinguishing between land cover types, the highest backscatter values occur when moisture is greater than 50%. When the moisture–backscatter relationship is examined for each land cover, the positive relationship remains; although most land covers are not coincident with high moisture, backscatter nevertheless increases with increasing moisture. Investigating the backscatter versus moisture relationship confirms that this trend is still observable from some land cover class observations that are not in close proximity to open water.

The data analysis shows that Ka-band backscatter is measurably sensitive to different classes of vegetation (volume scattering) evidenced by an examination of the LVIS LiDAR complexity. The shapes of the backscatter-complexity relationship are possibly due to differences between two-way transmissivity for different vegetation types and foliage orientations, providing more interesting lines of future inquiry.

Combining observed LiDAR surface complexity with surface moisture and reference land cover datasets provides a framework for a simple empirical scattering model, the KaPS, capable of simulating Ka-band backscatter returns from water and land surfaces, with implications for being used for inverse problems, to estimate moisture and surface complexity (vegetation types) from Ka-band backscatter. The majority of observed variations in the AirSWOT backscatter data can be reproduced using the KaPS model, as evidenced by the mean and median R^2 values of 0.74 and 0.72 in a "best case" or a "matching observations" scenario (see Fig. 9). Fig. 8 also shows that the worse performing land covers have mean absolute errors no greater than ~3 dB, which is similar to the GO model used by Fatras et al.. [21] for soil-only land covers at incidence angles less than 7°. This work additionally stands out as achieving this error range while including very diverse surface types, from open water, to exposed soils, and dense foliage.

The purpose of the KaPS model is to map how backscatter changes as a result of changing surface conditions, meaning the model is not expected to resemble the observations exactly, but should reflect the input reference data, as seen in Fig. 10(f). The model is highly sensitive to the input data, as desired, showing a tonally rough surface matching the complexities of the input data. As a result, spatial correlations with observations are low, while maintaining low MAE and RMSE values, demonstrating accurate approximations given relatively coarse resolution input data. Differences between the MAE and RMSE values of the model and the simulation performance versus observations can be explained by the relative percentage of each land cover type, as the reported mean and median model values weight all land covers equally, whereas some land cover types might be represented in different amounts over space.

Possible applications of this model include: 1) estimating areas and conditions where SWOT might have brighter than expected scattering–such as bright land in proximity to open water, confusing the open water area estimate, 2) estimating wetland area, 3) retrievals of skin-level canopy and soil moisture (called surface moisture here), 4) retrievals of vegetation structure, and 5) providing a first-guess of scattering conditions and planning for new Ka-band instruments, particularly focused on data acquisition over areas of uncertainty. Many of these applications will require the use and development of higher spatial and temporal resolution moisture and complexity data, which is an area of ongoing research.

There are several limitations of this analysis, including: 1) Because the Ka-band AirSWOT data examined in this study primarily observed Arctic-Boreal wetland regions, the distribution of scattering coefficients, particularly those found in Fig. 3, may be skewed to reflect wetter regions. To counter this effect and to understand how the scattering values may depart from those observed, this study describes how scattering varies over similar yet drier surfaces, and develops a simple model to simulate Ka-band radar backscatter to estimate the appearance of wetter and drier areas. 2) The expected moisture values underpinning the KaPS model are much coarser than ideal for this study. While this issue was addressed by adding in surface water features to give a larger range of moisture variability and higher resolution wet-dry transitions, variations across non-water surfaces remain limited to the scale of the original 25 km SMOPS resolution, so the dynamic range of moisture for non-land features is likely to be under-sampled as a result.

This research reveals that, under moderately wet summertime conditions, 1) the mean backscatter from open water, emergent aquatic vegetation, wet soils, and land vegetation classes vary by at least one standard deviation, making them all highly separable, with likely confusion with water occurring about 5% of the time, and 2) a simple model for near-nadir and low incidence Ka-band scattering can be used to simulate changes to natural surface complexity and dielectric constant (as complexity and surface moisture) under non-frozen conditions.

This study confirms expected relationships between moisture and backscatter, extends this examination to include structural variability, and develops the KaPS model. The performance of KaPS is similar to that of a previous GO modeling study [21] while including more diverse surface covers and higher incidence angles, up to 27°. This model produces the framework for developing a methodology to enable geophysical inversions using moisture and complexity (or vegetation type) from Ka-band measurements. Future applications for KaPS include further investigations of skin-surface moisture and complex surface impacts on Ka-band backscatter returns for terrestrial ecology and hydrology studies and increased confidence in AirSWOT and SWOT surface classification accuracies and water surface elevation retrievals.

APPENDIX

A. *SMOPS Soil Moisture Downscaling*

Daily NOAA SMOPS soil moisture data are spatially downscaled by adding reference water features from the Landsat-derived ADLC product. The SMOPS data are nearest-neighbor-resampled to 30 meters to match the ADLC, and the resampled SMOPS pixels corresponding to the ADLC open water class are re-assigned values of 100% moisture. Finally, the 30-m resampled and waterbody-added moisture data is aggregated to 1 km to increase computation speed for analysis. An additional 90-m product was developed for finer-detailed analysis and testing as the AirSWOT swath width is approximately 4 km. This

process produces products that visually show both the original 25 km large pixel shapes and finer ADLC water bodies. Note: Because the ADLC does not have a separate class for "snow", snow-capped mountain ranges are labeled "water" as seen in the Alaska Range in the south and the Brooks Range in the north. None of the AirSWOT lines in this analysis include snow cover. An example of this output is shown in Fig. 12.

B. Incidence Angle Backscatter Curve Look-up Table

TABLE I
SUBSET OF AN EXAMPLE INCIDENCE ANGLE BACKSCATTER CURVE LOOK-UP TABLE THAT IS USED TO ESTIMATE THE BACKSCATTER FOR THE OPEN WATER LAND COVER CLASS

Backscatter Incidence Angle Curve (incidence angle limited subset) for the "Open Water" Land Cover Class			
Incidence Angle [θ, degrees]	**Lower Bound [σ,dB] (32nd Percentile)**	**Mean [σ,dB]**	**Upper Bound [σ,dB] (68 nd Percentile)**
0.334247	12.93341	15.08547	16.51797
2.539372	12.05942	14.42304	15.94506
3.526987	11.60328	14.08157	15.64961
4.25216	11.23964	13.81227	15.41691
4.86377	10.91243	13.57254	15.21016
5.386985	10.61647	13.35811	15.02564
5.928993	10.29311	13.12672	14.8271
6.301115	10.06054	12.96234	14.68647
6.734053	9.778361	12.76539	14.51852
7.112991	9.520427	12.58797	14.3678
7.483919	9.257312	12.40974	14.21702
7.875642	8.967125	12.21666	14.05447
8.219593	8.701021	12.04305	13.90913
8.565874	8.421079	11.86257	13.7582
8.918208	8.121226	11.66382	13.58859
9.222013	7.850358	11.47967	13.42875
9.526209	7.567808	11.28395	13.25677
9.795744	7.307969	11.10159	13.09507
10.087	7.016959	10.89574	12.91141
10.33765	6.757565	10.71194	12.74686
10.61132	6.463914	10.50509	12.5616
10.86778	6.177281	10.3064	12.38423
11.1143	5.889039	10.11207	12.2121
11.37498	5.566982	9.9044	12.03068
11.6112	5.25516	9.715745	11.86935

The data is subset to show incidence angles 0.3-11 degrees (the full range is ~0- 27°). These values, and the values for other land covers, correspond to the percentile lines shown in Figure 3a in the main text. The KaPS simulator uses these percentile curves to simulate backscatter values beyond the 4-6 range that is estimated from the regression formulas shown in the following appendix table (Appendix Table II).Formulas Representing the relationships between Ka-band Backscatter and X, where X is Surface Moisture or LiDAR Complexity.

TABLE II
FORMULAS WITH WEIGHTS FOR THE COMPLEXITY AND MOISTURE COMPONENTS

Land Cover	Weight	Equation: x=Moisture [% Surface Moisture], Values [0-100]					
		intercept	x	x^2	x^3	x^4	x^5
Evergreen Forest	0.01	4736.75	-688.88	39.25	-1.1	0.01	0
Deciduous Forest	0.62	-4588.46	1010.97	-86.15	3.57	-0.07	0
Mixed Forest	0.54	1188.48	-179.33	10.42	-0.29	0	0
Woodland	0.01	13610.84	-2107.86	128.64	-3.87	0.06	0
Low Shrub	0.47	14062.98	-1779.11	82.91	-1.66	0.01	0
Tall Shrub	0.96	131052.81	-23515.83	1678.59	-59.6	1.05	-0.01
Open Shrub	0.41	-209.48	40.67	-2.75	0.08	0	0
Herbaceous	0.53	48615.05	-8092.93	535.71	-17.63	0.29	0
Tussock Tundra	0.99	843690.05	-145111.72	9952.42	-340.14	5.79	-0.04
Sparsely Vegetated	0.60	899228.13	-145952.06	9455.97	-305.7	4.93	-0.03
Fen	0.99	-1183.52	176.25	-10.75	0.33	-0.01	0
Bog	0.54	392.04	-35.3	1.22	-0.02	0	0
Shallow-Littoral	0.60	-98568.79	10964.51	-483.82	10.59	-0.12	0
Barren	0.63	35840.66	-3270.2	119.15	-2.17	0.02	0
Open Water	0.59	-2152844.8	124903.5	-2896.25	33.55	-0.19	0

Land Cover	Weight	Equation: x=Surface Complexity [unitless Complexity], Values [0-1]					
		intercept	x	x^2	x^3	x^4	x^5
Evergreen Forest	0.99	1205.19	-25586.88	215998.84	-892249.78	1794913.56	-1406302.05
Deciduous Forest	0.38	-317.34	5972.14	-40106.12	127522.46	-195712.12	117088.18
Mixed Forest	0.46	-309.96	6724.95	-52181.25	191965.38	-339337.8	231413.3
Woodland	0.99	5458.21	-126345.13	1154119.93	-5182984.04	11434359.91	-9919201.86
Low Shrub	0.53	141097.64	-4115223.06	47716493.42	-274992716.31	787802635.19	-897608964.69
Tall Shrub	0.04	10676.15	-250470.39	2320409.34	-10600896.23	23891455.51	-21267620.32
Open Shrub	0.59	714.79	-17202.22	164318.54	-765179.5	1727710.89	-1513302.79
Herbaceous	0.47	-7404.47	186044.92	-1831765.26	8829553.73	-20820687.64	19221575.28
Tussock Tundra	0.01	4173.81	-127184.21	1514596.22	-8809718.65	25042646.48	-27835274.63
Sparsely Vegetated	0.4	10227.1	-483626.02	7921774.4	-59892344.09	214884616.99	-296986717.36
Fen	0.01	8532.98	-212470.17	2096129.34	-10213961.78	24557554.82	-23306388.47
Bog	0.46	-18991.35	616549.27	-7940828.6	50737680.85	-160834884.79	202342333.3
Shallow-Littoral	0.4	72618.82	-2195097.73	26363580.55	-157154110.21	464756908.14	-545305819.32
Barren	0.37	-6047.77	173577.02	-1952119.11	10739797.52	-28852309.18	30274912.87
Open Water	0.41	4940271.26	-177334772.58	2543324236.96	-18217388409.99	65170712478.93	-93153334641.13

Each column represents the coefficients to be multiplied by the value of x^n. When the estimated backscatter values calculated for the moisture-only and complexity-only equations are combined using a weighted average, the 'best case' R^2 value has a wide range, with a mean value of 0.74

TABLE III
R^2, MAE [dB], AND RMSE [dB] VALUES ARE PRESENTED FOR WEIGHTED AND AVERAGED COMBINED EQUATIONS FOR STRUCTURAL COMPLEXITY AND MOISTURE RELATIONSHIPS WITH BACKSCATTER

Land Cover	**R^2 when Combined**	**MAE [dB]**	**RMSE [dB]**
Evergreen Forest	0.7278882	3.2788781	3.8894456
Deciduous Forest	0.5253822	3.3269223	4.4061073
Mixed Forest	0.8997592	1.6529752	2.4649654
Woodland	0.7145177	3.2369433	4.0599052
Low Shrub	0.6165528	3.3290047	4.5043288
Tall Shrub	0.7758107	2.5877106	3.0060137
Open Shrub	0.8640675	1.5685829	2.3952886
Herbaceous	0.6939242	3.5270336	4.5033925
Tussock Tundra	0.9284269	1.4822261	0.714637
Sparsely Vegetated	0.6428162	3.5547184	4.4075492
Fen	0.7839777	2.5358328	2.9885093
Bog	0.6931238	2.3131434	3.0055778
Shallow-Littoral	0.7174921	3.2479175	4.8195844
Barren	0.743683	3.2218391	4.0598658
Open Water	0.8248593	2.3570233	3.067109
Mean	0.7434854	2.7480501	3.486152
Median	0.7278882	3.2218391	3.8894456

TABLE IV
EXAMPLE LOOK-UP TABLE IS SHOWN HERE, REPRESENTING THE OPEN WATER CLASS WHERE MOISTURE VARIES ALONGSIDE EXPECTED VALUES FOR BACKSCATTER

Mean [σ , dB]	**Mean [moisture,%]**	**St.dev [moisture,%]**	**N**
-1.58456	77.46552	26.18773	58
-1.03527	80.67857	23.57616	84
-0.41428	79.44604	24.89024	139
0.206599	79.97576	24.9934	165
0.82869	77.73276	26.53263	232
1.43599	79.81301	25.76657	246
2.050704	84.4939	23.32551	328
2.667682	84.13759	22.6418	407
3.269233	83.60879	22.87557	455
3.888232	82.96468	24.69955	538
4.498026	85.09425	21.84071	626
5.106603	85.66619	22.25574	704
5.713768	87.48333	20.803	720
6.320185	85.88547	22.33674	812
6.946563	88.51372	19.89841	911
7.551043	88,06116	20.53167	981
8.163685	88.2756	19.91512	918
8.78386	87.38308	21.18018	1052
9.391719	87.659	20.79142	1000
10.007	89.28021	19.19452	1117
10.60923	89.83412	18.70408	1278
11.21332	90.33612	17.83365	1315
11.85064	90.38787	18.40762	1534
12.47023	91.24403	17.60969	1844
13.0978	94.3606	14.01129	3178
13.68909	94.91729	13.6202	5042
14.33307	97.10643	10.29683	8635
14.90723	97.8522	8.69686	10311
15.50393	97.98239	8.474852	10393
16.1045	97.97534	8.486458	9285
16.71226	97,60107	8.915389	7470
17.32706	97.43703	9.32157	5661
17.93788	97.47845	9.427794	4107
18.55645	97.41703	9.264411	2736
19.17067	98.03393	7.924339	1945
19.78232	98.27338	7,881548	1251
20.37361	98.74349	5.622926	768
20.9804	98.30789	7.268499	380
21.58409	98.03509	8.449083	171
22.22585	99.18667	2.555827	75

Pixels having lower moisture values low water fraction have a high moisture standard deviation and are correlated with lower backscatter, likely due to the mixture of land and vegetation.

TABLE V
RESULTS OF THE SPATIAL COMPARISON BETWEEN THE SIMULATED KA-BAND BACKSCATTER DATA USING THE KAPS MODEL AND THE OBSERVED KA-BAND BACKSCATTER DATA FROM AIRSWOT

Simulation Type	R^2	MAE [dB]	RMSE [dB]
Simulated -10%Wet -10%Complex	0.24868	1.816496	2.47142
Simulated -10%Wet -20%Complex	0.277411	2.038861	2.957338
Simulated -10%Wet 0%Complex	0.285369	1.567955	2.035293
Simulated -10%Wet 10%Complex	0.265718	1.526052	2.031412
Simulated -10%Wet 20%Complex	0.260489	2.058388	2.521526
Simulated -20%Wet -10%Complex	0.281416	1.59276	2.083844
Simulated -20%Wet -20%Complex	0.252773	1.83788	2.48883
Simulated -20%Wet 0%Complex	0.285058	1.568108	2.035583
Simulated -20%Wet 10%Complex	0.27239	1.648857	2.115735
Simulated -20%Wet 20%Complex	0.264257	1.523177	2.028708
Simulated 0%Wet -10%Complex	0.281021	2.034259	2.972458
Simulated 0%Wet -20%Complex	0.280808	2.034111	2.972526
Simulated 0%Wet 0%Complex	0.259457	1.791121	2.596978
Simulated 0%Wet 10%Complex	0.22494	2.333794	2.786155
Simulated 0%Wet 20%Complex	0.225001	2.334197	2.786445
Simulated 10%Wet -10%Complex	0.263319	2.840405	3.523234
Simulated 10%Wet -20%Complex	0.26097	2.760976	3.501387
Simulated 10%Wet 0%Complex	0.250107	2.800393	3.529452
Simulated 10%Wet 10%Complex	0.236871	2.48206	3.105019
Simulated 10%Wet 20%Complex	0.229419	2.316214	2.774965
Simulated 20%Wet -10%Complex	0.255145	2.721559	3.47954
Simulated 20%Wet -20%Complex	0.262483	2.841344	3.52446
Simulated 20%Wet 0%Complex	0.249865	2.801242	3.529987
Simulated 20%Wet 10%Complex	0.245478	2.763209	3.4788
Simulated 20%Wet 20%Complex	0.243335	2.469461	3.090874

"Simulated % Wet and % Complex" values correspond to increasing or decreasing moisture content and structural complexity of the model input reference data to produce the simulations. R^2 values are low mostly due to the differences in the model output resolution, being 10x larger (~36m) than the AirSWOT observations (3.6m).

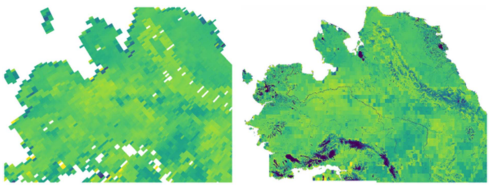

Fig. 12. Water bodies are added to the NOAA SMOPS Soil Moisture product for comparison with higher-resolution Ka-band backscatter data. ***On the left*** is a map of the NOAA SMOPS 25 km soil moisture product covering parts of Alaska and Canada; ***on the right*** is the 1 km downscaled data, including water bodies produced in this study.

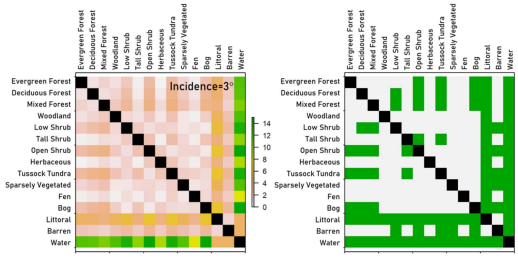

Fig. 13. Separability matrix from Fig. 4 is included here again on the left for reference– on the right, the binary thresholding of the separability matrix for values greater than 2 is shown, highlighted in green. These figures demonstrate that water and the littoral zones are separable from all other land cover classes and that some other land cover classes can be distinguished between themselves (open shrubs and low shrubs are noticeably different from tall forest classes).

ACKNOWLEDGMENT

The 2017 ABoVE AirSWOT data was processed using software developed at the Jet Propulsion Laboratory; the authors would like to thank the author of the InSAR software, Xiaoqing Wu, for contributing to the production of the data and supporting this study. A portion of this work was performed at the Jet Propulsion Laboratory, California Institute of Technology, under contract with NASA.

REFERENCES

[1] L. C. Smith, "Satellite remote sensing of river inundation area, stage, and discharge: A review," *Hydrological Processes*, vol. 11, pp. 1427–1439, 1997.
[2] D. E. Alsdorf and D. P. Lettenmaier, "Tracking fresh water from space," *Science*, vol. 301, no. 5639, pp. 1491–1494, Sep. 2003, doi: 10.1126/science.1089802.
[3] D. E. Alsdorf, E. Rodríguez, and D. P. Lettenmaier, "Measuring surface water from space," *Rev. Geophys.*, vol. 45, no. 2, 2007, Art. no. 123, doi: 10.1029/2006RG000197.
[4] G. Schumann, P. D. Bates, M. S. Horritt, P. Matgen, and F. Pappenberger, "Progress in integration of remote sensing–Derived flood extent and stage data and hydraulic models," *Rev. Geophys.*, vol. 47, no. 4, 2009, Art. no. 240125, doi: 10.1029/2008rg000274.
[5] J. - F. Crétaux et al., "Flood mapping inferred from remote sensing data," *Int. Water Technol. J.*, vol. no. 1, 2011, Art. no. 13.
[6] S. W. Cooley, L. C. Smith, J. C. Ryan, L. H. Pitcher, and T. M. Pavelsky, "Arctic-boreal lake dynamics revealed using cubesat imagery," *Geophysical Res. Lett.*, vol. 46, no. 4, pp. 2111–2120, 2019, doi: 10.1029/2018gl081584.
[7] S. W. Cooley, J. C. Ryan, and L. C. Smith, "Human alteration of global surface water storage variability," *Nature*, vol. 591, pp. 78–81, 2021, doi: 10.1038/s41586-021-03262-3.
[8] R. P. De Frasson, G. J.-P. Schumann, A. J. Kettner, G. R. Brakenridge, and W. F. Krajewski, "Will the surface water and ocean topography (SWOT) satellite mission observe floods?," *Geophysical Res. Lett.*, vol. 46, no. 17–18, pp. 10435–10445, 2019, doi: 10.1029/2019gl084686.
[9] E. S. Kasischke, J. M. Melack, and M. C. Dobson, "The use of imaging radars for ecological applications—A review," *Remote Sens. Environ.*, vol. 59, no. 2, pp. 141–156, Feb. 1997, doi: 10.1016/S0034-4257(96)00148-4.
[10] L. L. Hess, J. M. Melack, E. M. L. M. Novo, C. C. F. Barbosa, and M. Gastil, "Dual-season mapping of wetland inundation and vegetation for the central amazon basin," *Remote Sens. Environ.*, vol. 87, no. 4, pp. 404–428, Nov. 2003, doi: 10.1016/J.Rse.2003.04.001.
[11] E. D. Kyzivat et al., "A high-resolution airborne color-infrared camera water mask for the nasa above campaign," *Remote Sens.*, vol. 11, no. 18, Jan. 2019, Art. no. 18, doi: 10.3390/Rs11182163.
[12] S. Biancamaria, D. P. Lettenmaier, and T. M. Pavelsky, "The SWOT mission and its capabilities for land hydrology," *Surv. Geophys*, vol. 37, no. 2, pp. 307–337, Mar. 2016, doi: 10.1007/s10712-015-9346-y.
[13] S. Wdowinski, S. - W. Kim, F. Amelung, T. H. Dixon, F. Miralles-Wilhelm, and R. Sonenshein, "Space-based detection of wetlands' surface water level changes from L-band SAR interferometry," *Remote Sens. Environ.*, vol. 112, no. 3, pp. 681–696, Mar. 2008, doi: 10.1016/j.rse.2007.06.008.
[14] S. - H. Hong, S. Wdowinski, S. - W. Kim, and J. - S. Won, "Multitemporal monitoring of wetland water levels in the Florida Everglades using interferometric synthetic aperture radar (InSAR)," *Remote Sens. Environ.*, vol. 114, no. 11, pp. 2436–2447, Nov. 2010, doi: 10.1016/j.rse.2010.05.019.
[15] J. - W. Kim, Z. Lu, J. W. Jones, C. K. Shum, H. Lee, and Y. Jia, "Monitoring everglades freshwater marsh water level synthetic aperture radar backscatter," *Remote Sens. Environ.*, vol. 150, pp. 66–81, Jul. 2014, doi: 10.1016/j.rse.2014.03.031.
[16] K. Bakian-Dogaheh, R. H. Chen, Y. Yi, J. S. Kimball, M. Moghaddam, and A. Tabatabaeenejad, "A model to characterize soil moisture and organic matter profiles in the permafrost active layer in support of radar remote sensing in Alaskan Arctic tundra," *Environ. Res. Lett.*, vol. 17, 2022, Art. no. 025011, doi: 10.1088/1748-9326/ac4e37.
[17] R. Fjørtoft et al., "Karin - the ka-band radar interferometer on SWOT: Measurement principle, processing and data specificities," in *Proc. IEEE Int. Geosci. Remote Sens. Symp.*, 2010, pp. 4823–4826, doi: 10.1109/IGARSS.2010.5650601.
[18] X. Wu, S. Hensley, E. Rodriguez, D. Moller, R. Muellerschoen, and T. Michel, "Near nadir ka-band sar interferometry: SWOT airborne experiment," in *Proc. IEEE Int. Geosci. Remote Sens. Symp.*, 2011, pp. 2681–2684, doi: 10.1109/IGARSS.2011.6049755.

[19] R. Fjørtoft et al., "Karin - The ka-band radar interferometer on SWOT: Measurement principle, processing and data specificities," in *Proc. IEEE Int. Geosci. Remote Sens. Symp.*, 2010, Ppp. 4823–4826, doi: 10.1109/IGARSS.2010.5650601.

[20] F. Frappart et al., "Preliminary assessment of SARAL/altika observations over the ganges-brahmaputra and irrawaddy rivers," *Mar. Geodesy*, vol. 38, no. sup1, pp. 568–580, Sep. 2015, doi: 10.1080/01490419.2014.990591.

[21] C. Fatras et al., "Radar backscattering coefficient over bare soils at ka-band close to nadir angle," *IEEE Geosci. Remote Sens. Lett.*, vol. 13, no. 9, pp. 1290–1294, Sep. 2016, doi: 10.1109/LGRS.2016.2582382.

[22] M. Durand, L. - L. Fu, D. P. Lettenmaier, D. E. Alsdorf, E. Rodriguez, and D. Esteban-Fernandez, "The surface water and ocean topography mission: Observing terrestrial surface water and oceanic submesoscale eddies," *Proc. IEEE*, vol. 98, no. 5, pp. 766–779, May 2010, doi: 10.1109/Jproc.2010.2043031.

[23] E. Peral and D. Esteban-Fernandez, "SWOT mission performance and error budget," in *Proc. IEEE Int. Geosci. Remote Sens. Symp.*, 2018, pp. 8625–8628, doi: 10.1109/IGARSS.2018.8517385.

[24] M. Durand, L. - L. Fu, D. P. Lettenmaier, D. E. Alsdorf, E. Rodriguez, and D. Esteban-Fernandez, "The surface water and ocean topography mission: Observing terrestrial surface water and oceanic submesoscale eddies," *Proc. IEEE*, vol. 98, no. 5, pp. 766–779, May 2010, doi: 10.1109/Jproc.2010.2043031.

[25] D. Moller, E. Rodriguez, J. Carswell, and D. Esteban-Fernandez, "AirSWOT- A calibration/validation platform for the SWOT mission," in *Proc. Int. Geosci. Remote Sens. Symp.*, 2010, pp. 2010.

[26] R. Fjørtoft et al., "KaRIn on SWOT: Characteristics of near-nadir ka-band interferometric SAR imagery," *IEEE Trans. Geosci. Remote Sens.*, vol. 52, no. 4, pp. 2172–2185, Apr. 2014, doi: 10.1109/TGRS.2013.2258402.

[27] S. Lobry, L. Denis, B. Williams, R. Fjørtoft, and F. Tupin, "Water detection in SWOT HR images based on multiple Markov random fields," *IEEE J. Sel. Topics Appl. Earth Observ. Remote Sens.*, vol. 12, no. 11, pp. 4315–4326, Nov. 2019, doi: 10.1109/JSTARS.2019.2948788.

[28] J. V. Fayne and L. C. Smith, "Characterization of near-nadir ka-band scattering from wet surfaces," in *Proc. IEEE Int. Geosci. Remote Sens. Symp.*, 2021, pp. 6132–6135, doi: 10.1109/IGARSS47720.2021.9553413.

[29] L. C. Smith and A. L. Et, "AirSWOT Ka-band returns over edwards AFB wetlands (piute ponds)," in *Proc. SWOT Sci. Definition Team Meeting*, 2014, Art. no. 20254.

[30] O. Baney, "First airswot ka-band radar backscatter returns over a complex california wetland," in *Proc. AGU Fall Meeting*, 2014, Art. no. 20251. Accessed: Jul. 17, 2021. [Online]. Available: https://agu.confex.com/agu/fm14/webprogram/Paper9131.html

[31] L. Smith, J. Fayne, and E. Kzivat, "Prelimin'17 NASA above airswot flight campaigns," 2018. [Online]. Available: https://Spark.Adobe.Com/Page/Qsah6yjwral1s

[32] T. Hagfors, "Relationship of geometric optics and autocorrelation approaches to the analysis of lunar and planetary radar," *J. Geophysical Res.*, vol. 71, no. 2, pp. 379–383, 1966, doi: 10.1029/JZ071i002p00379.

[33] D. E. Barrick, "Relationship between slope probability density function and the physical optics integral in rough surface scattering," *Proc. IEEE*, vol. 56, no. 10, pp. 1728–1729, Oct. 1968, doi: 10.1109/PROC.1968.6718.

[34] R. S. Longhurst, *Geometrical and Physical Optics*, 3rd ed.. London, U.K.: Addison-Wesley Longman Ltd, 1974.

[35] A. Moreira, P. Prats-Iraola, M. Younis, G. Krieger, I. Hajnsek, and K. P. Papathanassiou, "A tutorial on synthetic aperture radar," *IEEE Geosci. Remote Sens. Mag.*, vol. 1, no. 1, pp. 6–43, Mar. 2013, doi: 10.1109/MGRS.2013.2248301.

[36] Y. Oh, K. Sarabandi, and F. T. Ulaby, "An empirical model and an inversion technique for radar scattering from bare soil surfaces," *IEEE Trans. Geosci. Remote Sens.*, vol. 30, no. 2, pp. 370–381, Mar. 1992, doi: 10.1109/36.134086.

[37] P. C. Dubois, J. J. Van Zyl, and T. Engman, "Measuring soil moisture with imaging radars," *IEEE Trans. Geosci. Remote Sens*, vol. 33, no. 4, pp. 915–926, Jul. 1995.

[38] A. Nashashibi, F. T. Ulaby, and K. Sarabandi, "Measurement and modeling of the millimeter-wave backscatter response of soil surfaces," *IEEE Trans. Geosci. Remote Sens.*, vol. 34, no. 2, pp. 561–572, Mar. 1996, doi: 10.1109/36.485132.

[39] O. Boisot, F. Nouguier, B. Chapron, and C. - A. Guérin, "The GO4 model in near-nadir microwave scattering from the sea surface," *IEEE Trans. Geosci. Remote Sens.*, vol. 53, no. 11, pp. 5889–5900, Nov. 2015, doi: 10.1109/TGRS.2015.2424714.

[40] O. Boisot et al., "Ka-band backscattering from water surface at small incidence: A wind-wave tank study," *J. Geophysical Res.: Oceans*, vol. 120, no. 5, pp. 3261–3285, 2015, doi: 10.1002/2014JC010338.

[41] J. Bergeron, G. Siles, R. Leconte, M. Trudel, D. Desroches, and D. L. Peters, "Assessing the capabilities of the surface water and ocean topography (SWOT) mission for large lake water surface elevation monitoring under different wind conditions," *Hydrol. Earth System Sci.*, vol. 24, no. 12, pp. 5985–6000, Dec. 2020, doi: 10.5194/hess-24-5985-2020.

[42] F. T. Ulaby and W. Herschel Stiles, "Microwave response of snow," *Adv. Space Res.*, vol. 1, no. 10, pp. 131–149, Jan. 1981, doi: 10.1016/0273-1177(81)90389-6.

[43] L. Zhang, J. Shi, Z. Zhang, and K. Zhao, "The estimation of dielectric constant of frozen soil-water mixture at microwave bands," in *Proc. IEEE Int. Geosci. Remote Sens. Symp.*, 2003, pp. 2903–2905, doi: 10.1109/IGARSS.2003.1294626.

[44] V. L. Mironov and Y. I. Lukin, "Temperature dependable microwave dielectric model for frozen soils," *PIERS Online*, vol. 5, no. 5, pp. 406–410, 2009, doi: 10.2529/PIERS090220040026.

[45] N. Baghdadi, H. Bazzi, M. El Hajj, and M. Zribi, "Detection of frozen soil using Sentinel-1 SAR data," *Remote Sens.*, vol. 10, no. 8, Aug. 2018, Art. no. 1182, doi: 10.3390/rs10081182.

[46] T. Jackson, "Effects of soil properties on microwave dielectric constants," *Transportation Research Record*, 1987, Accessed: Aug. 03, 2021. [Online]. Available: https://www.semanticscholar.org/paper/EFFECTS-OF-SOIL-PROPERTIES-ON-MICROWAVE-DIELECTRIC-Jackson/72e785e95f4b7313004eb993cf9da30908a3a21b

[47] N. Short, A. - M. Leblanc, W. Sladen, G. Oldenborger, V. Mathon-Dufour, and B. Brisco, "Radarsat-2 D-insar for ground displacement in permafrost terrain, validation from Iqaluit airport, Baffin island, Canada," *Remote Sens. Environ.*, vol. 141, pp. 40–51, Feb. 2014, doi: 10.1016/J.Rse.2013.10.016.

[48] F. Mohammadimanesh, B. Salehi, M. Mahdianpari, B. Brisco, and M. Motagh, "Multi-temporal, multi-frequency, and multi-polarization coherence and sar backscatter analysis of wetlands," *ISPRS J. Photogrammetry Remote Sens.*, vol. 142, pp. 78–93, Aug. 2018, doi: 10.1016/J.Isprsjprs.2018.05.009.

[49] B. Brisco et al., "Evaluation of C-band SAR for identification of flooded vegetation in emergency response products," *Can. J. Remote Sens.*, vol. 45, no. 1, pp. 73–87, Jan. 2019, doi: 10.1080/07038992.2019.1612236.

[50] T. - H. Liao, M. Simard, M. Denbina, and M. P. Lamb, "Monitoring water level change and seasonal vegetation change in the coastal wetlands of louisiana using L-band time-series," *Remote Sens.*, vol. 12, no. 15, Jan. 2020, Art. no. 15, doi: 10.3390/Rs12152351.

[51] S. - B. Kim and T. - H. Liao, "Robust retrieval of soil moisture at field scale across wide-ranging SAR incidence angles for soybean, wheat, forage, oat and grass," *Remote Sens. Environ.*, vol. 266, Dec. 2021, Art. no. 112712, doi: 10.1016/j.rse.2021.112712.

[52] J. V. Fayne et al., "Airborne observations of arctic-boreal water surface elevations from AirSWOT Ka-Band InSAR and LVIS LiDAR," *Environ. Res. Lett.*, vol. 15, no. 10, Oct. 2020, Art. no. 105005, doi: 10.1088/1748-9326/abadcc.

[53] N. M. Desrochers et al., "Effects of aquatic and emergent riparian vegetation on SWOT mission capability in detecting surface water extent," *IEEE J. Sel. Topics Appl. Earth Observ. Remote Sens.*, vol. 14, pp. 12467–12478, 2021, doi: 10.1109/JSTARS.2021.3128133.

[54] E. H. Altenau et al., "AirSWOT measurements of river water surface elevation and slope: Tanana river, AK," *Geophysical Res. Lett.*, vol. 44, no. 1, pp. 181–189, 2017, doi: 10.1002/2016GL071577.

[55] L. H. Pitcher et al., "AirSWOT InSAR mapping of surface water elevations and hydraulic gradients across the Yukon flats basin, Alaska," *Water Resour. Res.*, vol. 55, no. 2, pp. 937–953, 2019, doi: 10.1029/2018WR023274.

[56] E. H. Altenau et al., "Temporal variations in river water surface elevation and slope captured by AirSWOT," *Remote Sens. Environ.*, vol. 224, pp. 304–316, Apr. 2019, doi: 10.1016/j.rse.2019.02.002.

[57] S. Tuozzolo et al., "Estimating river discharge with swath altimetry: A proof of concept using AirSWOT observations," *Geophysical Res. Lett.*, vol. 46, no. 3, pp. 1459–1466, 2019, doi: 10.1029/2018GL080771.

[58] M. Denbina, M. Simard, E. Rodriguez, X. Wu, A. Chen, and T. Pavelsky, "Mapping water surface elevation and slope in the mississippi river delta using the AirSWOT ka-band interferometric synthetic aperture radar," *Remote Sens.*, vol. 11, no. 23, Jan. 2019, Art. no. 2739, doi: 10.3390/rs11232739.

[59] J. V. Fayne, L. C. Smith, L. H. Pitcher, and T. M. Pavelsky, "Above: Airswot ka-band radar over surface waters of Alaska and Canada, 2017," *ORNL DAAC*, Mar. 2019, [Online]. Available: https://doi.Org/10.3334/ORNLdaac/1646

[60] J. A. Wang, D. Sulla-Menashe, C. E. Woodcock, O. Sonnentag, R. F. Keeling, and M. A. Friedl, "Above: Landsat-derived annual dominant land cover across above core domain, 1984-2014," *Glob. Change Biol.*, vol. 26, pp. 807–822, 2019, doi: 10.3334/ORNLdaac/1691.
[61] C. R. Grant and B. S. Yaplee, "Back scattering from water and land at centimeter and millimeter wavelengths," *Proc. IRE*, vol. 45, no. 7, pp. 976–982, Jul. 1957, doi: 10.1109/Jrproc.1957.278508.
[62] W. P. Waite and H. C. Macdonald, "'Vegetation penetration' with k-band imaging radars," *IEEE Trans. Geosci. Electron.*, vol. 9, no. 3, pp. 147–155, Jul. 1971, doi: 10.1109/Tge.1971.271487.
[63] E. Rodriguez, D. E. Fernandez, E. Peral, C. W. Chen, J.-W. D. Bleser, and B. Williams, "Wide-swath altimetry: A review," in *Satellite Altimetry over Oceans and Land Surfaces*. Boca Raton, FL, USA: CRC Press, 2017.
[64] U. D. Of C. N. N. E. S. D. and I. S. O. Of S. and P. Operations, "NOAA's office of satellite and product operations," Accessed: Jan. 25, 2021. [Online]. Available: https://Www.Ospo.Noaa.Gov/Products/Land/Smops/
[65] J. B. Blair, D. L. Rabine, and M. A. Hofton, "The laser vegetation imaging sensor: A medium-altitude, digitisation-only, airborne laser altimeter for mapping vegetation and topography," *ISPRS J. Photogrammetry Remote Sens.*, vol. 54, no. 2–3, pp. 115–122, 1999, doi: 10.1016/S0924-2716(99)00002-7.
[66] P. Hyde et al., "Mapping forest structure for wildlife habitat analysis using waveform lidar: Validation of montane ecosystems," *Remote Sens. Environ.*, vol. 96, no. 3, pp. 427–437, Jun. 2005, doi: 10.1016/j.rse.2005.03.005.
[67] J. B. Blair and M. Hofton, *ABoVE LVIS L2 Geolocated Surface Elevation Product, Version 1. [LVIS LiDAR Complexity]*. Boulder, CO, USA. NASA National Snow and Ice Data Center Distributed Active Archive Center, 2018, doi: 10.5067/IA5WAX7K3YGY.[2021].
[68] H. Tang and J. Armston, *GEDI L2B Footprint Canopy Cover and Vertical Profile Metrics*. Sioux Falls, SD, USA: LP DAAC, 2022, Art. no. 39.
[69] I. G. Cumming and J. J. Van Zyl, "Feature utility in polarimetric radar image classification," in *Proc. 12th Can. Symp. Remote Sens. Geosci. Remote Sens. Symp.*, 1989, pp. 1841–1846, doi: 10.1109/IGARSS.1989.576569.
[70] N. Baghdadi, M. Bernier, R. Gauthier, and I. Neeson, "Evaluation of C-band SAR data for wetlands mapping," *Int. J. Remote Sens.*, vol. 22, no. 1, pp. 71–88, Jan. 2001, doi: 10.1080/014311601750038857.
[71] M. T. Hallikainen, F. T. Ulaby, M. C. Dobson, M. A. El-Rayes, and L. Wu, "Microwave dielectric behavior of wet soil-part 1: Empirical models and experimental Observations," *IEEE Trans. Geosci. Remote Sens.*, vol. Ge-23, no. 1, pp. 25–34, Jan. 1985, doi: 10.1109/Tgrs.1985.289497.
[72] E. W. Hoen and H. A. Zebker, "Topography-driven variations in backscatter strength and depth observed over the Greenland ice sheet with Insar," in *Proc. IEEE Int. Geosci. Remote Sens. Symp. Taking Pulse Planet, Role Remote Sens. Manag. Environ. Proc.*, 2000, pp. 470–472, doi: 10.1109/IGARSS.2000.861599.
[73] E. Van Zyl, "Nature and properties of electromagnetic waves," in *Introduction to the Physics and Techniques of Remote Sensing*. Hoboken, NJ, USA: Wiley, 2006, pp. 23–50, doi: 10.1002/0471783390.ch2.
[74] J. J. van Zyl, "Unsupervised classification of scattering behavior using radar polarimetry data," *IEEE Trans. Geosci. Remote Sens.*, vol. 27, no. 1, pp. 36–45, Jan. 1989, doi: 10.1109/36.20273.
[75] J. V. Fayne and L. C. Smith, "How does wind influence near-nadir and low-incidence Ka-band radar backscatter and coherence from small inland water bodies?," *MDPI Remote Sens.*, vol. 15, 2023, Art. no. 3361, doi: 10.3390/rs15133361.

Jessica V. Fayne (Member, IEEE) received the M.S. degree in geography and geoinformation science from George Mason University, Fairfax, Virginia, USA, in 2015 and the Ph.D. degree in geography from the University of California, Los Angeles, USA, in 2022.

She worked as a Contractor for NASA Goddard Space Flight Center (GSFC) 2014–2017 and as a Research Associate for the University of South Carolina, School of Earth, Ocean and Environment (2015–2017), studying improving and calibrating remotely sensed observations of water cycle variables including surface water and soil moisture. From 2017–2022, she was a Visiting Student Researcher at NASA Jet Propulsion Laboratory (JPL). She is currently an Assistant Professor at the University of Michigan in the Department of Earth and Environmental Science.

Laurence C. Smith received the Ph.D. degree in Earth and atmospheric sciences from Cornell University, Ithaca, NY, USA, in 1996.

He is the John Atwater and Diana Nelson University Professor of Environmental Studies and Professor of Earth, Environmental and Planetary Sciences at Brown University. His research interests include the Arctic, hydrology, satellite remote-sensing technologies, and climate change.

Dr. Smith was named a Guggenheim Fellow by the John S. Guggenheim Foundation in 2006 and 2007. In 2015, he was elected a Fellow of the American Geophysical Union.

Tien-Hao Liao received the Ph.D. degree in electrical engineering from the University of Washington, Seattle, USA, in 2015.

Following this, he served as a Research Fellow at the Radiation Laboratory, University of Michigan. His primary research interests lie in the development of electromagnetic scattering models for natural terrain, waveguides, and topological photonics. His work has been instrumental in advancing microwave remote sensing techniques for vegetated and rough surfaces, particularly in the context of soil moisture retrieval for the NASA SMAP mission. In addition, he has made contributions to the application of L-band interferometry in wetland studies, showcasing its potential for the upcoming NISAR mission. His contributions to the field were recognized with a NASA Postdoctoral Program fellowship for research conducted in collaboration with the Jet Propulsion Laboratory (JPL).

Dr. Liao currently holds a faculty position at Taipei Tech in Taiwan.

Lincoln H Pitcher received the B.S., M.S., and Ph.D. degrees in geography from the University of California, Los Angeles, in 2007, 2013, and 2019, respectively.

As a Postdoctoral Scholar and Visiting Fellow at the Earth Science and Observation Center (ESOC) of the Cooperative Institute for Research and Environmental Sciences (CIRES) at the University of Colorado, Boulder, he uses optical and radar remote sensing techniques to understand hydrological surface dynamics.

Michael Denbina received the B.Sc. degree in electrical engineering, in 2010, and the Ph.D. degree in geomatics engineering with a specialization in earth observation, in 2015, from the University of Calgary, Calgary, AB, Canada.

In 2015, he became a NASA Postdoctoral Program Fellow with the NASA Jet Propulsion Laboratory (JPL) in Pasadena, CA, USA. During his fellowship, he primarily worked on the mapping of vegetation height and structure using polarimetric SAR interferometry. In 2017, he joined JPL as a Signal Analysis Engineer in the Radar Science and Engineering Section. His research interests include algorithms for the retrieval of many types of environmental parameters from SAR interferometry and polarimetry, such as forest canopy height, biomass, and surface water level.

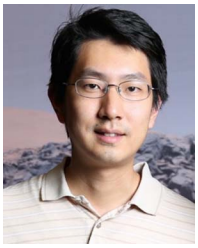

Albert C. Chen received the B.S.E. degree from the University of Michigan, Ann Arbor, USA, in 2006 and the M.S. and Ph.D. degrees from Stanford University, Stanford, CA, in 2008 and 2013, all in electrical engineering.

As a Postdoctoral Scholar at Stanford Department of Geophysics, he studied permafrost in Alaska using both repeat-pass InSAR and ground-penetrating radar. He is currently a Signal Analysis Engineer, joining the Radar System and Instrument Engineering Section of NASA Jet Propulsion Laboratory (JPL) in Pasadena, CA, USA in 2015. His current research interests include interferometric synthetic aperture radar remote sensing, signal processing, and scientific computation.

Marc Simard received the M.Sc. degree in physics and the Ph.D. degree in geomatics from the Université Laval, Quebec, QC, Canada, in 1994 and 1998, respectively.

He is currently a Senior Research Scientist with NASA Jet Propulsion Laboratory, Pasadena, CA, USA. His research focuses on the development and use of radar remote sensing technology to understand the role of large-scale climatic and hydrogeomorphic processes on vegetation structure, with a particular emphasis on coastal regions. He has contributed to and led the development of new multi-instrument airborne and satellite remote sensing techniques to measure the hydrology and sediment transport in coastal ecosystems and to monitor vegetation and hydrology of forested and coastal landscapes for projects such as Delta-X (leader), and NISAR and SWOT (contributor).

Curtis W. Chen received the B.S. and A.B. degrees in electrical engineering and political science and the M.S. and Ph.D. degrees in electrical engineering from Stanford University, Stanford, CA, USA, in 1996, 1999, and 2001, respectively.

He developed new algorithms for 2-D phase unwrapping of interferometric SAR data. Since 2001, he has been with NASA Jet Propulsion Laboratory, Pasadena, CA, USA, where he has been involved in radars for Mars landers and Earth-science instruments. He was the Lead System Engineer of the Soil Moisture Active Passive combined active/passive instrument system from subsystem integration through launch.

Brent A. Williams (Member, IEEE) received the Ph.D. degree in electrical and computer engineering from Brigham Young University, Provo, UT, USA, in 2010.

He is currently a member of the Radar Algorithms and Processing Group, NASA Jet Propulsion Laboratory, California Institute of Technology, Pasadena, CA, USA. He is the Algorithm Development Lead for the SWOT science processor that performs water detection, phase unwrapping, layover flagging, and geolocation of high-resolution interferometric data.